AD-A155 425 CHEYENNE MOUNTAIN LATE TIME SIMULATION RESULTS(U) NAVAL 1/1
RESEARCH LAB WASHINGTON DC K HAIN ET AL. 07 JUN 85
NRL-MR-5565

UNCLASSIFIED F/G 18/3 NL

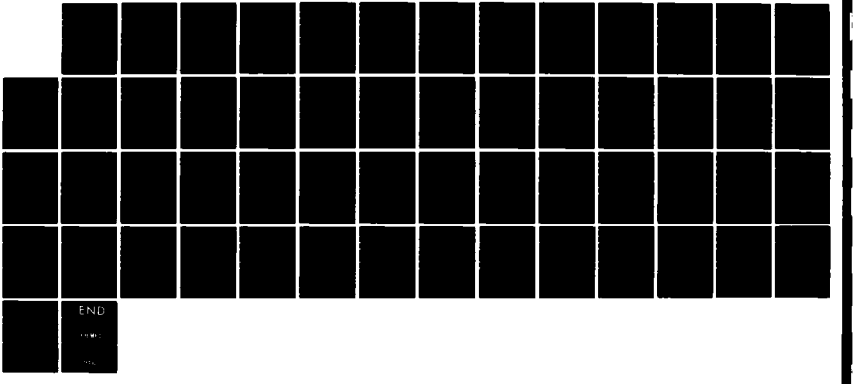

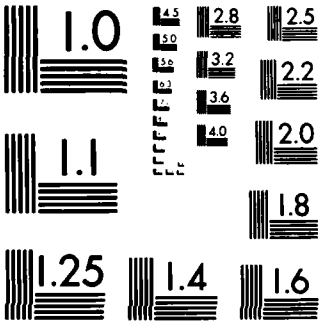

NRL Memorandum Report 5565

Cheyenne Mountain Late Time Simulation Results

K. HAIN, G. HAIN AND J. A. FEDDER

Geophysical and Plasma Dynamics Branch
Plasma Physics Division

June 7, 1985

This research was sponsored by the Defense Nuclear Agency under Subtask S99QMXBC, work unit 00118 and work unit title "Late Time Electrostatic."

NAVAL RESEARCH LABORATORY
Washington, D.C.

SECURITY CLASSIFICATION OF THIS PAGE

REPORT DOCUMENTATION PAGE

1a REPORT SECURITY CLASSIFICATION UNCLASSIFIED	1b RESTRICTIVE MARKINGS
2a SECURITY CLASSIFICATION AUTHORITY	3 DISTRIBUTION/AVAILABILITY OF REPORT Approved for public release; distribution unlimited.
2b DECLASSIFICATION/DOWNGRADING SCHEDULE	
4 PERFORMING ORGANIZATION REPORT NUMBER(S) NRL Memorandum Report 5565	5 MONITORING ORGANIZATION REPORT NUMBER(S)
6a NAME OF PERFORMING ORGANIZATION Naval Research Laboratory 6b OFFICE SYMBOL (If applicable) Code 4780	7a NAME OF MONITORING ORGANIZATION
6c ADDRESS (City, State, and ZIP Code) Washington, DC 20375-5000	7b ADDRESS (City, State, and ZIP Code)
8a NAME OF FUNDING/SPONSORING ORGANIZATION Defense Nuclear Agency 8b OFFICE SYMBOL (If applicable) RAAE	9 PROCUREMENT INSTRUMENT IDENTIFICATION NUMBER
8c ADDRESS (City, State, and ZIP Code) Washington, DC 20305	10 SOURCE OF FUNDING NUMBERS PROGRAM ELEMENT NO: 62715H; PROJECT NO; TASK NO.; WORK UNIT ACCESSION NO: DN320-100

11 TITLE (Include Security Classification)
Cheyenne Mountain Late Time Simulation Results

12 PERSONAL AUTHOR(S)
Hain, K., Hain, G. and Fedder, J.A.

13a TYPE OF REPORT	13b TIME COVERED	14 DATE OF REPORT (Year, Month, Day)	15 PAGE COUNT
Interim	FROM 10/83 TO 9/84	1985 June 7	56

16 SUPPLEMENTARY NOTATION
This research was sponsored by the Defense Nuclear Agency under Subtask S99QMXBC, work unit 00118 and work unit title "Late Time Electrostatic."

17 COSATI CODES			18 SUBJECT TERMS (Continue on reverse if necessary and identify by block number)
FIELD	GROUP	SUB-GROUP	HANE, Nuclear simulation, Nuclear weapons phenomenology, Late-time electrostatic

19 ABSTRACT (Continue on reverse if necessary and identify by block number)

In this report we present results for the late time evolution of the Cheyenne Mountain nuclear explosion scenario. Results are presented from both the DEMAG simulation code and the MELT simulation code. The results are compared and the differences between them are explained. We conclude that the simulation results are in good agreement.

20 DISTRIBUTION/AVAILABILITY OF ABSTRACT	21 ABSTRACT SECURITY CLASSIFICATION
☒ UNCLASSIFIED/UNLIMITED ☐ SAME AS RPT ☐ DTIC USERS	UNCLASSIFIED
22a NAME OF RESPONSIBLE INDIVIDUAL J. D. Huba	22b TELEPHONE (Include Area Code) (202) 767-3630 22c OFFICE SYMBOL Code 4780

DD FORM 1473, 84 MAR 83 APR edition may be used until exhausted
All other editions are obsolete

SECURITY CLASSIFICATION OF THIS PAGE

CONTENTS

CHEYENNE MOUNTAIN LATE TIME SIMULATION RESULTS

I. INTRODUCTION

The Cheyenne Mountain nuclear detonation scenario involved a high altitude (> 150 km), large yield (> 1 M ton) nuclear explosion over the central Rocky Mountain region of the U.S. Such high altitude nuclear explosions (HANE) evolve through a number of temporal stages during which the physical description of the explosion and the effects are radically different from each other. For the simulation results presented in this report we are concerned with the last and longest period of evolution of a HANE; a period, hours in length, when the vast amount of plasma created in the explosion slowly evolves, and the ionosphere and magnetosphere return to their pre-burst condition.

The computer codes which have been developed to study the period are commonly termed "late-time electrostatic codes". There are two of these codes: the NRL code DEMAG and the MRC code MELT. The codes are "late time" because they simulate HANE phenomenology later than about 5 min after detonation. They are termed "electrostatic" because plasma motion perpendicular to the geomagnetic field is treated in terms of an electrostatic potential field. The theory for the perpendicular plasma transport for the DEMAG code has been reported in Hain and Fedder (1984). The theory for the parallel plasma transport is the usual hydrodynamic theory. The theory for the MELT code has been previously reported in Longmire and Kilb (1977) and Kilb (1977).

In this report we will discuss and compare the two codes DEMAG and MELT which use very different algorithms. We will show results of simulations from each code for the Cheyenne Mountain scenario during the

Manuscript approved February 25, 1985.

temporal period of 5 to 30 minutes after burst. We will discuss the results pointing out similarities and differences between them. Finally we will briefly summarize these results and present our conclusions.

II. CODE DESCRIPTION

Although both codes, DEMAG and MELT, are designed to solve an identical set of theoretical equations, the numerical algorithms used are considerably different. The DEMAG numerical algorithm used for both neutral atmosphere and plasma transport is an "Eulerian" algorithm; the numerical grid is a constant fixed mesh. Both the plasma and the neutral gas are transported across the grid from mesh point to mesh point. The MELT code uses a "Lagrangian" algorithm for the plasma transport. That is, as plasma is transported from point to point in space, the numerical mesh points are moved along with the plasma and the same parcel of plasma remains within the same numerical cell. The neutral atmosphere in the MELT code uses a fixed "Eulerian" mesh as does the DEMAG code.

Figures 1 and 2 show the DEMAG fixed meshes for the plasma and the neutral gas, respectively, on a geomagnetic meridional plane in the Northern hemisphere. For the plasma (Fig. 1) the coordinate lines are magnetic field lines and magnetic potential lines. For the neutral gas (Fig. 2) the coordinate lines are an adapted coordinate system which tends toward a magnetic orientation at high altitudes and is spherical at low altitudes; the coordinate system is described mathematically in Appendix A. In each case the third coordinate is the rotational coordinate about the magnetic axis. Figure 3 is a similar diagram to Fig. 1 except it shows the MELT plasma mesh. Here one can clearly see the magnetic field line coordinate but the coordinate along the field is unequally spaced and is controlled by the motion of plasma along the field line. The MELT neutral

atmosphere mesh is an earth centered spherical mesh which terminates at 1500 km altitude and is not shown here.

The choice of numerical meshes for the simulations is controlled by a number of considerations. The spherical nature of the neutral atmosphere at low altitudes is required to allow the burst disrupted atmosphere to return to a sensible hydrostatic equilibrium. The distortion of the DEMAG neutral mesh at higher altitudes towards a geomagnetic mesh is designed to allow a better description of neutral gas motion as it is carried to high altitudes by the plasma.

Both codes, DEMAG and MELT, make use of a geomagnetic field aligned mesh for the plasma owing to consideration of the electrostatic nature of the plasma transport at late times. For electrostatic plasma transport the magnetic field is considered to be constant. Moreover, plasma motion perpendicular to the field has a very special property; specifically, all plasma on a common field line (more correctly contained in a common flux tube) at a particular moment of time remains on a common field line (in a common flux tube) for all time. The plasma is said to be "frozen" to the field. A geomagnetic field line coordinate therefore is a natural choice for the plasma mesh.

The DEMAG choice of "Eulerian" transport on the geomagnetic mesh involved two considerations. First, it was felt that modern numerical methods were sufficiently accurate to adequately control numerical errors and to maintain a good approximation to the field frozen plasma motion described above. Second, Eulerian transport is inherently simpler in multiple dimensions because of the fixed numerical grid, and in such large codes, simplicity is an advantage where obtainable. The MELT code has the advantage that the Lagrangian transport exactly satisfies the field frozen plasma motion until the numerical grid becomes too distorted for further

computation. At this point the grid must be restructured which is a complex and difficult operation, and to some undetermined extent violates the field frozen condition thereby partially negating its initial advantage.

Clearly there are many possible choices to be made when developing simulation codes as complex and difficult as DEMAG and MELT. Different people will make different choices and all for good reasons. It is therefore not too surprising that two very different codes have been developed to simulate the same types of HANE problems. The quality of the codes and the different approaches can only be tested by comparing simulation results to data. In the absence of hard data, which is almost non-existent for late time HANE, the quality of simulations can only be verified by comparing results from different codes. In the case of two very different codes such as DEMAG and MELT such a comparison of results can provide a verity to the results which would otherwise be totally unattainable.

III. RESULTS

In this report we show results from both the DEMAG and MELT simulations for the Cheyenne Mountain HANE scenario for the time period 300 to 1800 seconds after burst. The two simulation codes where initialized at 300 seconds with the same data set which was generated by MRC with the MICE MHD nuclear simulation code.

At 300 sec the initial blast wave from the burst has propagated far from the burst point. The large cavity in the geomagnetic field has collapsed and the magnetic field has returned to ambient values. The remnant of the HANE is a large, geomagnetic field aligned plume of plasma which extends from the northern conjugate to the southern conjugate

ionosphere. The lower portion of this plasma plume with plasma densities greater than 10^8 cm^{-3} is shown in Figs. 4 and 5. The plasma in the plume is moving at high velocities along the field lines in order to achieve a hydrostatic equilibrium and at lower altitudes in response to strong upward neutral atmospheric heave winds. The still highly disturbed neutral atmospheric densities are shown in Figs. 6 and 7. The geomagnetic field lines which contain the plasma plume pass through the equatorial plane of the magnetosphere at altitudes above one earth radius. Figure 8 which shows a contour diagram of the field line integrated densities at the geomagnetic equator shows the great size of the plasma plume at high altitudes. It is more than 2000 km in width and 4000 km in depth perpendicular to the geomagnetic field.

During the simulation the plasma in the geomagnetic field aligned plume evolves. It loses density via recombination at low altitudes in the ionosphere. The plasma moves up and down along the field lines in response to pressure and gravity forces, and also in response to the neutral atmosphere heave winds. Motion of the plume perpendicular to the geomagnetic field occurs due to gravity forces, centrifugal forces, coriolis forces, and neutral wind friction forces. The motions along the field and recombination slowly deplete the plume plasma density, while motions perpendicular to the field distort and stretch the plume onto higher latitude flux tubes or compress the plume onto lower latitude flux tubes. The plume can also drift slowly relative to the earth's rotation.

The cumulative effects of these processes on the plasma plume can be seen in Figs. 9-11 while the relaxation of the neutral atmosphere to near ambient density is seen in Fig. 12. In studying the plasma density in Figs. 9 and 10 it is noted that the maximum plasma density in the plume has

fallen by about a factor of 3 in one half hour. The plume has moved poleward (northern plume northward - southern plume southward) about 600 km. Moreover, the poleward border of the plasma plume is more diffuse and has a considerably reduced density gradient. A better picture of the poleward motion can be seen by comparing the result in Fig. 11 with the initialization in Fig. 8. In this comparison it is seen that the eastward and westward portions of the plume plasma has remained almost stationary while the center has moved upward in the equatorial plane. The motion in the ionosphere is similar. The eastward and westward portion of the plumes remain almost stationary while the center of the plume moves poleward. A comparison of Figs. 9-11 shows that the field frozen plasma motion results in higher velocities at high altitudes. As the plume moves 600 km poleward in the ionosphere the equatorial portion of the plume moves 3000 km higher.

Figures 13 and 14 show MELT results for the plasma density at 1800 secs; they are to be compared to Figs. 9 and 10 of the DEMAG results. One first notices that the maximum plasma densities in the two sets of results are very nearly the same, and that both plasma plumes appear to be decaying in a similar manner. There are, however, some differences. The poleward density gradient in the MELT results is much sharper than in DEMAG. This difference could be a result of the different numerical algorithms, that is, a result of the Eulerian algorithm in DEMAG allowing more diffusion across the geomagnetic field: or it could be the result of the more evolved poleward plume motion in DEMAG. The DEMAG plasma plume moves about twice as far poleward as does the plume in the MELT simulation. The difference in poleward motion of the two plumes will be discussed more fully later as it appears to be the major difference between the simulation results.

Comparisons between the results of the simulations for other plasma and atmospheric properties can be carried out by using the microfiche. The fiche contain plasma and neutral densities, pressure, and temperature; species densities; and plasma and neutral motions. The DEMAG results are shown starting with initial conditions at 300 sec intervals between 300 and 1800 sec. The MELT results are shown at 600 sec intervals between 600 and 1800 secs. A description of the fiche figures and layout is contained in Appendix B.

IV. DISCUSSION

The DEMAG and MELT results shown on the fiche have been compared to each other between 600 and 1800 sec. The comparison of data shows an overall agreement between results, particularly if one is interested in the high plasma density regions of the plume. Results for plasma and neutral densities, temperatures and species densities are all very similar and are approximately equal. The primary difference between the results involves the poleward and upward motion of the plume. The DEMAG plume moves faster and about twice as far poleward as the MELT plume. We think this difference in motion perpendicular to the geomagnetic field has a straightforward explanation which follows.

In both DEMAG and MELT the primary forces driving plasma motion perpendicular to the geomagnetic field are neutral drag, caused by atmospheric heave and relaxation; centrifugal forces, caused by rapid plasma motion along the curved geomagnetic field in the plume; and gravitational attraction, pulling the plasma plume downward and equatorward. For the Cheyenne Mountain simulation these three forces are initially in a very sensitive balance: the neutral drag and centrifugal

forces pushing upward, and gravity pulling downward. If either of the codes emphasizes or diminishes one of these forces relative to the other code, we would expect a difference in motion owing to alterations in the sensitive balance of the driving forces.

Figures 15 and 16 show potential plots for DEMAG and MELT, respectively, at 600 secs. Plasma flow is along the potential contours perpendicular to the geomagnetic field. The potential contours are shown on the geomagnetic equatorial plane. The reader will notice immediately that the contours near the boundaries in the two figures are decidedly different. The difference arises due to different boundary conditions for DEMAG and MELT but are not significant to the results since motion in these regions involves only incompressible flow of almost uniform ambient background ionosphere. Near the center of the plots the flow lines are much more similar.

The DEMAG results (Fig. 15) show three different regions of flow in the plasma plume. Between 6000 and 8000 km altitude there is strong upward flow near the center plane of the plume. The upward flow turns outward and then downward near the edges of the plume. This region of flow is driven by a local dominance of the centrifugal force term. At higher altitudes between 9,000 and 11,000 km the flow throughout the central portion of the plume is downward. This downward flow region is driven by a local dominance of the gravitational force term. Finally, in the highest portion of the plume, between 11,000 and 14,000 km, the flow near the central plane is again upward and is controlled by a local dominance of the neutral drag force term. (The neutral drag does not occur at these equatorial altitudes but takes place at the poleward border of the plume at lower altitudes.)

Similar flow features can be seen in the MELT results (Fig. 16). The low altitude upward flow occurs between 5500 and 7500 km altitudes. The downward flow occurs throughout the central portion of the plume between 8000 and 11,000 km. Above 11,000 km the downward flow is substantially weakened, where the DEMAG results show upward flow. These results can possibly be seen more clearly in the velocity vector diagrams shown in Figs. 17 and 18 for DEMAG and MELT, respectively.

The primary areas of disagreement in these results relate to the absence of upward flows at the highest altitudes in the MELT results and to the faster downward flow in the central plume shown in the MELT results relative to those of DEMAG. The reason for these differences is shown in Figs. 19-22.

Figures 19 and 20 show the neutral atmospheric densities on the central meridional plane at 600 sec for both the northern and southern conjugate regions. Of particular interest is the large atmospheric density above 1500 km altitude (the top of the MELT neutral grid) which occurs in both hemispheres. The high neutral density, because of its great extent along the geomagnetic field, can be very effective in enhancing the neutral drag force term in DEMAG relative to that in MELT. Figures 21 and 22 show that the neutral velocities at these high altitudes are primarily upward and poleward relative to the geomagnetic field, and therefore the enhanced neutral drag force term would strengthen upward and poleward plume motion. Since this force occurs at altitudes above 1500 km the MELT results do not account for it and therefore the MELT plume experiences less poleward acceleration. Increasing the MELT neutral atmospheric grid to roughly double its present height would be expected to bring the results into much closer agreement.

At 1800 secs, Figs. 23 and 24 show potential contours and Figs. 25 and 26 show velocity vectors for DEMAG and MELT, respectively. At this late time the plasma plumes in both results are moving primarily upward and poleward. The DEMAG plasma which began moving poleward earlier and more strongly continues to move slightly faster. This continuing difference in the results can again be traced back to the more dominant neutral drag force than in the DEMAG simulation at earlier times. At this time, the centrifugal force term is dominant and is forcing the upward and poleward motion. As the plasma motion in the plume parallel to the geomagnetic field slows and relaxes, gravitational forces will eventually dominate and will then cause the plume to fall and move equatorward. Since the DEMAG plume moves further poleward the DEMAG results indicate a more lengthy return to equilibrium than do the MELT results. More complete analysis of the complex perpendicular motion and the delicate balance of forces can be undertaken by study of the fiche entitled "POT". The fiche show potentials, velocities and force terms for the DEMAG simulations. The "POT" fiche are described in Appendix C.

In summary, we would conclude that the DEMAG and MELT simulations of the Cheyenne Mountain scenario are in good agreement. The primary disagreement involving perpendicular motion is understood and has been explained. We have also discussed the implications of that disagreement for later time evolution of the plasma plume. Both codes DEMAG and MELT appear to provide reasonably accurate results for the late time evolution of a high altitude nuclear explosion.

ACKNOWLEDGMENT

This research has been supported by the Defense Nuclear Agency.

Appendix A

This appendix discusses the derivation of the NRL DEMAG coordinate system for the neutral atmosphere. For reasons discussed in the text, this coordinate systems tends to dipolar magnetic coordinates at high altitudes and tends to a spherical coordinate system at low altitudes.

We consider a function of $f(y, r, \theta) = 0$ where y is a coordinate line description, r is the geocentric radius normalized to the earth radius and θ is the geomagnetic colatitude. Moreover, we require f to be a monotone function of r and θ, for η positive. The unit vectors perpendicular to η are given by

$$e_r = \frac{\partial f}{\partial r} \Big/ \sqrt{\left(\partial f/\partial r\right)^2 + \left(1/r \ \partial f/\partial \theta\right)^2}$$

$$e_\theta = \frac{1}{r}\frac{\partial f}{\partial \theta} \Big/ \sqrt{\left(\partial f/\partial r\right)^2 + \left(1/r \ \partial f/\partial \theta\right)^2}.$$

We now require that

$$e_r = 0 \text{ at } r = 1 \text{ (earths surface)}$$

$$e_\theta = 0 \text{ at } \theta = \frac{\pi}{2} \text{ (magnetic equator)}$$

A simple function which satisfies these conditions is

$$f = \frac{(r-1)^\varepsilon}{(\eta-1)^{\varepsilon-1}} - \left(\eta \sin^2\theta - 1\right) \text{ for } \varepsilon > 1.$$

For $\varepsilon = 1$, f describes a dipolar coordinate line; whereas for $\varepsilon = \infty$, f describes a radial coordinate line. For the DEMAG neutral mesh, we use $\varepsilon = 2$.

To numerically generate the grid we construct a coordinate line through the burst point and compute its total length. We subdivide this coordinate line to obtain one set of coordinates and then construct an orthogonal mesh to each side of this base coordinate line. The resulting mesh is displayed in figure 2.

The neutral boundary conditions are reflecting at 100 km altitude and out-flow on the other boundaries.

Appendix B

Tables B1 and B2 show the layout of the plots on the microfiche for the DEMAG and MELT results, respectively. The NRL fiche show the DEMAG results at 300 sec intervals between 300 and 1800 sec. The MRC fiche show the MELT results at 600 sec intervals between 600 and 1800 sec.

The quantities N_e, $v_\perp$, and Ψ are the field line integrated density, the perpendicular to B velocity and the electrostatic potential, respectively, plotted on the geomagnetic equatorial plane. n, P, and T are the density, pressure, and temperature, respectively. (N), (S), and (V) indicate the northern conjugate, southern conjugate meridional plane, and a vertical plane 5300 km north of the equator through the burst region and perpendicular to the central meridional plane. Subscripts e, p, i, N and v indicate electrons, plasma, ions, neutrals, and N_2 vibrational state, respectively.

Individual constituents enclosed in brackets, such as $[N^+]$ indicate species concentrations. A arrow, →, designates a vector plot and a star, *, signifies an expanded view of the burst and conjugate regions. A double star, **, indicates a unit vector plot to show flow directions. For the vertical plane velocities, v_x, v_y, and v_z show velocities in the meridional, longitudinal and vertical direction, respectively. For the MRC fiche a parallel, ∥, designates velocities parallel to the magnetic field.

All quantities are plotted in cgs units.

Table B1—NRL CHEYENNE

	$n_e(S)$	$T_e(N)$	$[O_2^+](S)$	$\overset{*}{n}_N(S)$	$T_n(S)$	$[N_2](N)$	$\overset{**}{\vec{v}}_n(N)$	$v_y(V)$
Title	$\overset{*}{n}_e(S)$	$T_i(S)$	$[O)_2^+(N)$	$\overset{*}{n}_N(N)$	$T_v(N)$	$[O_2](S)$	$\lvert v_N \rvert$	$v_z(V)$
Plasma grid	$\overset{*}{n}_e(N)$	$T_i(N)$	$[NO^+](S)$	$n_N(N)$	$[N](S)$	$[O_2](N)$	$n_N(V)$	$\lvert v_N \rvert(V)$
Neutral grid	$n_e(N)$	$[N^+](S)$	$[NO^+](N)$	$P_N(S)$	$[N](N)$	$[NO](S)$	$P_N(V)$	$\vec{v}_N(V)$
N_e	$P_p(S)$	$[N^+](N)$	$v_p(S)$	$P_N(N)$	$[O](S)$	$[NO](N)$	$T_N(V)$	
$\vec{v}_\perp$	$P_p(N)$	$[O^+](S)$	$\vec{v}_p(N)$	$T_N(S)$	$[O](N)$	$\vec{v}_n(S)$	$T_v(V)$	
Ψ	$T_e(S)$	$[O^+](N)$	$n_N(S)$	$T_N(N)$	$[N_2](S)$	$\vec{v}_n(N)$	$v_x(V)$	

Table B2--MRC CHEYENNE

	$n_e(S)$	$T_e(N)$	$[NO^+](S)$	$\overset{*}{n}_N(S)$	$T_v(S)$	$[N_2](N)$	$\overset{**}{\vec{v}}_n(N)$	$v_y(V)$
Title	$\overset{*}{n}_e(S)$	$T_i(S)$	$[NO^+](N)$	$\overset{*}{n}_N(N)$	$T_v(N)$	$[O_2](S)$	$\lvert v_N \rvert$	$v_z(V)$
Plasma grid	$\overset{*}{n}_e(N)$	$T_i(N)$	$[H^+](S)$	$n_N(N)$	$[N](S)$	$[O_2](N)$	$n_N(V)$	$\lvert v_N \rvert(V)$
Neutral grid	$n_e(N)$	$[N^+](S)$	$[H^+](N)$	$P_N(S)$	$[N](N)$	$[NO](S)$	$P_N(V)$	$\vec{v}_N(V)$
N_e	$P_p(S)$	$[N^+](N)$	$v_p^{\parallel}(S)$	$P_N(N)$	$[O](S)$	$[NO](N)$	$T_N(V)$	
$\vec{v}\perp$	$P_p(N)$	$[O^+](S)$	$v_p^{\parallel}(N)$	$T_N(S)$	$[O](N)$	$\vec{v}_n(S)$	$T_v(V)$	
Ψ	$T_e(S)$	$[O^+](N)$	$n_N(S)$	$T_N(N)$	$[N_2](S)$	$\vec{v}_n(N)$	$v_x(V)$	

Appendix C

The POT fiche show quantities related to the electrostatic potential equation. The organization of the fiche are shown in Table C1. The quantities presented are field line integrated and are shown on the geomagnetic equatorial plane. Various quantities are described by a series of letters which indicate their identity. First letters D, T, and F signify ion-neutral drag or friction forces: transport forces including the convective derivative, coriolis forces, and centrifugal forces; and body forces including the pressure gradient and gravity, respectively. The second letters P and H indicate Pedersen and Hall components, respectively. The subscripts 1 and 2 indicate the meridional and longitudinal components, respectively. The sum of the forces are signified by S1 amd S2 where S1 = DP2 + TP2 + FP2 + DH1 + $TH_{\perp}$ + FH1 and S2 = DP1 + TP1 + FP1 + DH2 + TH2 + FH2. The symbol R shows the divergence of S. The symbols C and E signify the capacitance and conductivity matrices, respectively, with the subscripts indicating which matrix element.

The theory and derivations for the quantities in the POT fiche are fully described in Hain and Fedder (1984).

Table C1—NRL POT CHEY

	DP_2	TH_2	C_{11}
Title	TP_2	FH_2	C_{22}
'	FP_2	S_1	C_{12}
$\vec{v}_1$	DH_1	S_2	E_{11}
DP_1	TH_1	$v_1 S_1$	E_{22}
TP_1	FH_1	$v_2 S_2$	E_{12}
FP_1	DH_2	R	

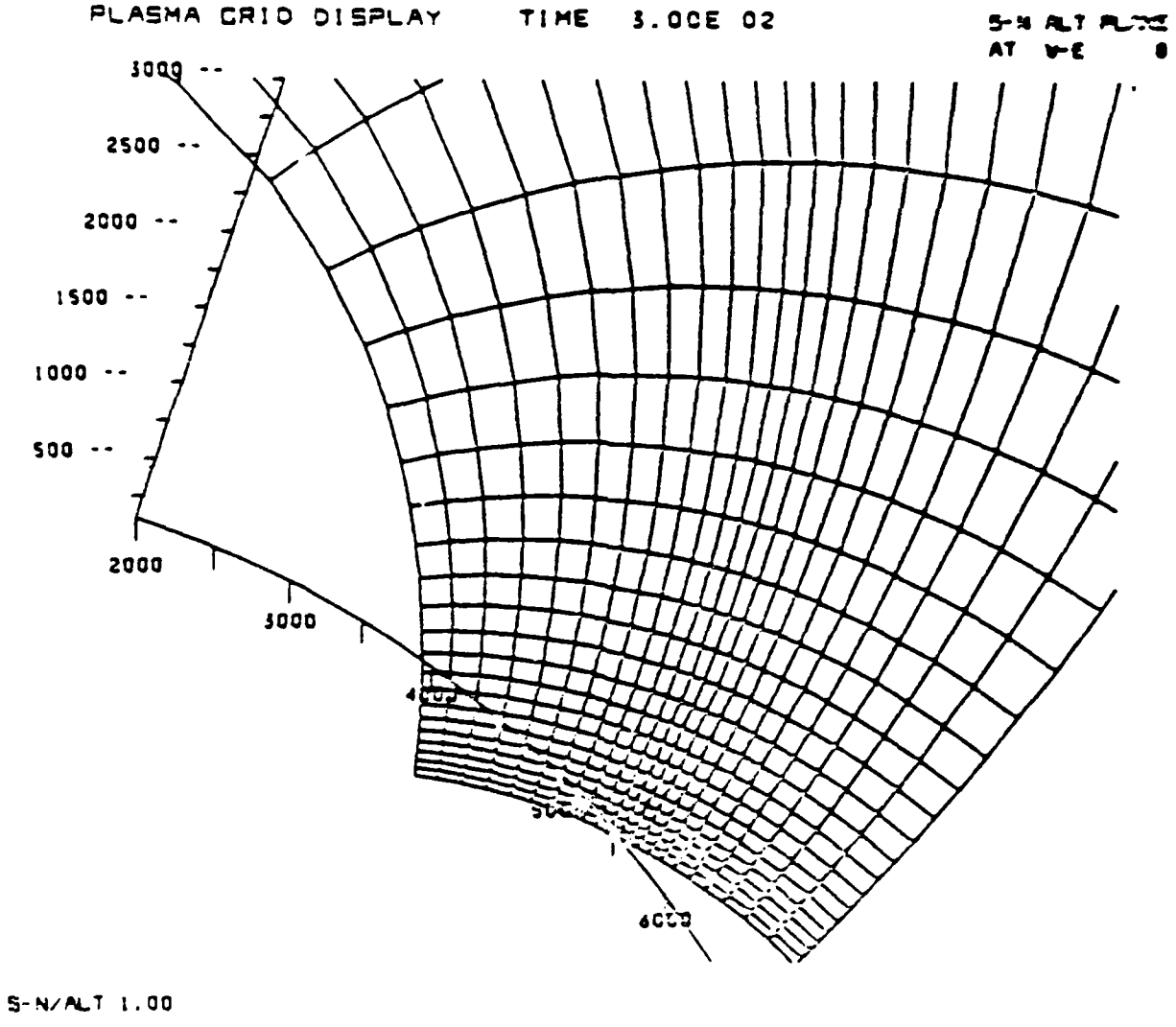

Figure 1. A plot of the geomagnetic field aligned plasma grid for the DEMAG code on a meridional plane in the northern conjugate region. The vertical scale is altitude and the horizontal scale is distance from the geomagnetic equator along the earth's surface in kilometers.

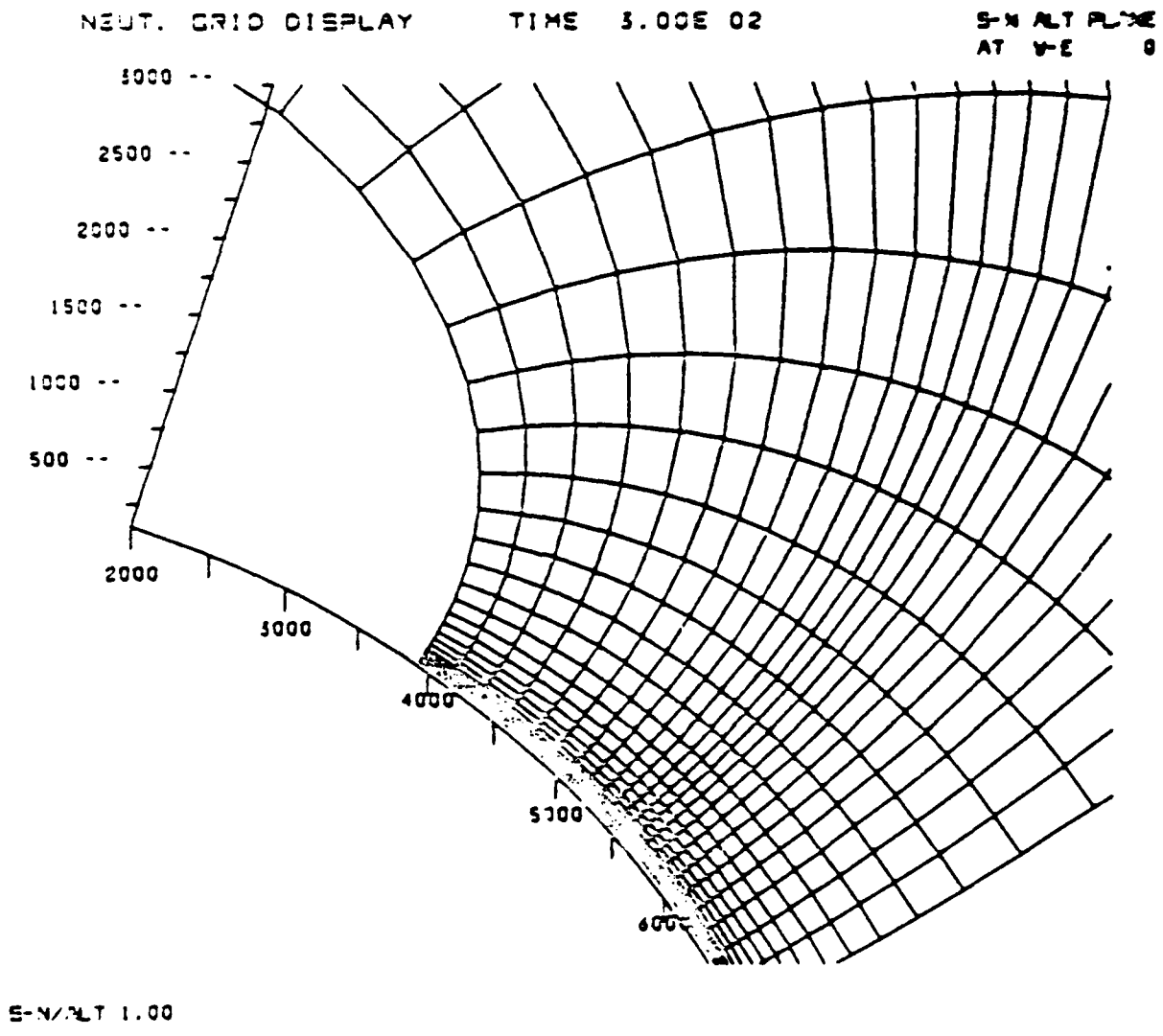

Figure 2. A plot of the neutral atmosphere grid for the DEMAG code on a meridional plane in the northern conjugate region. The vertical and horizontal scales are identical to those in Figure 1.

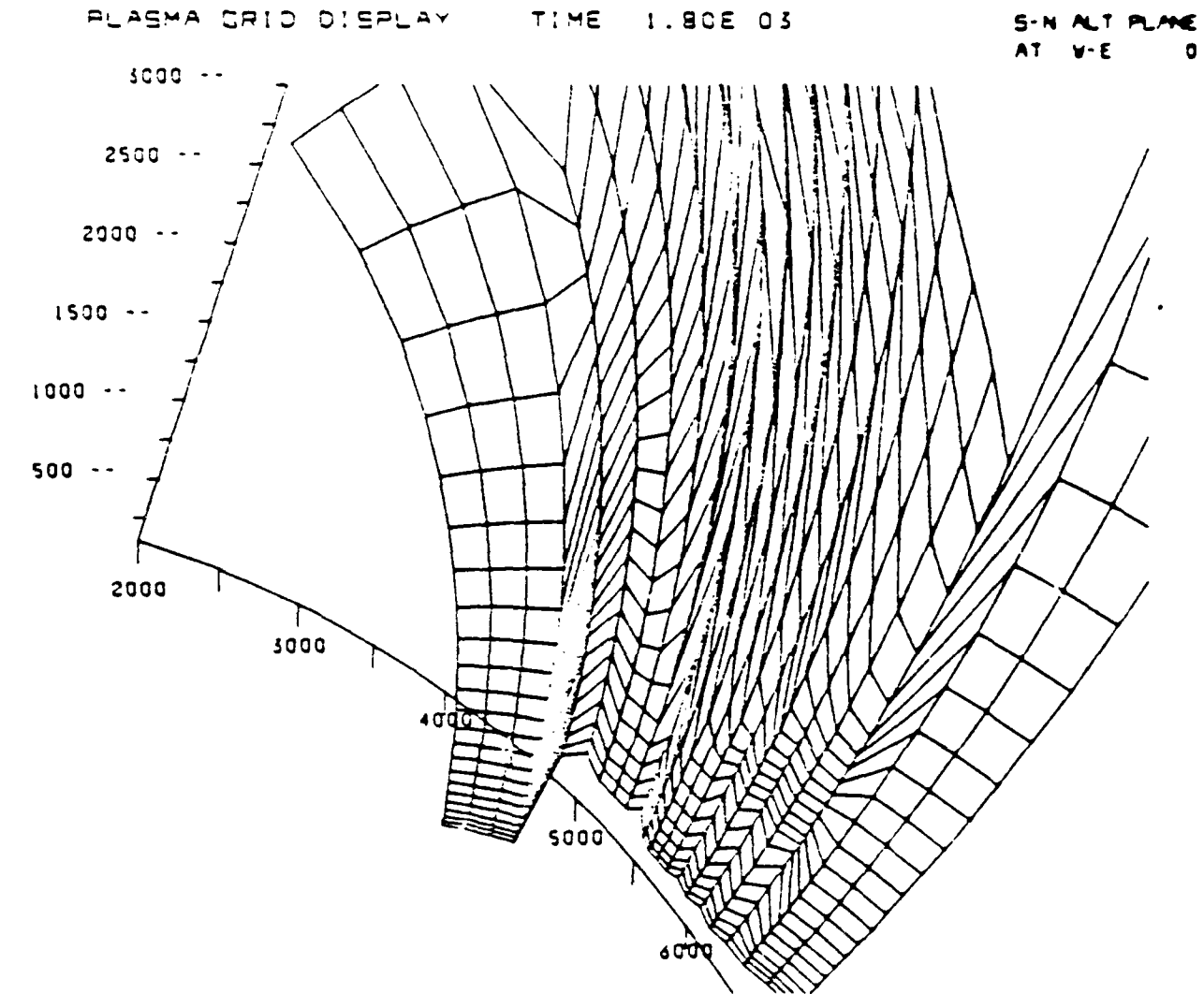

Figure 3. A plot of the "Lagrangian" geomagnetic field aligned plasma grid for the MELT code on a meridional plane in the northern conjugate. The vertical and horizontal scales are identical to those in Figure 1.

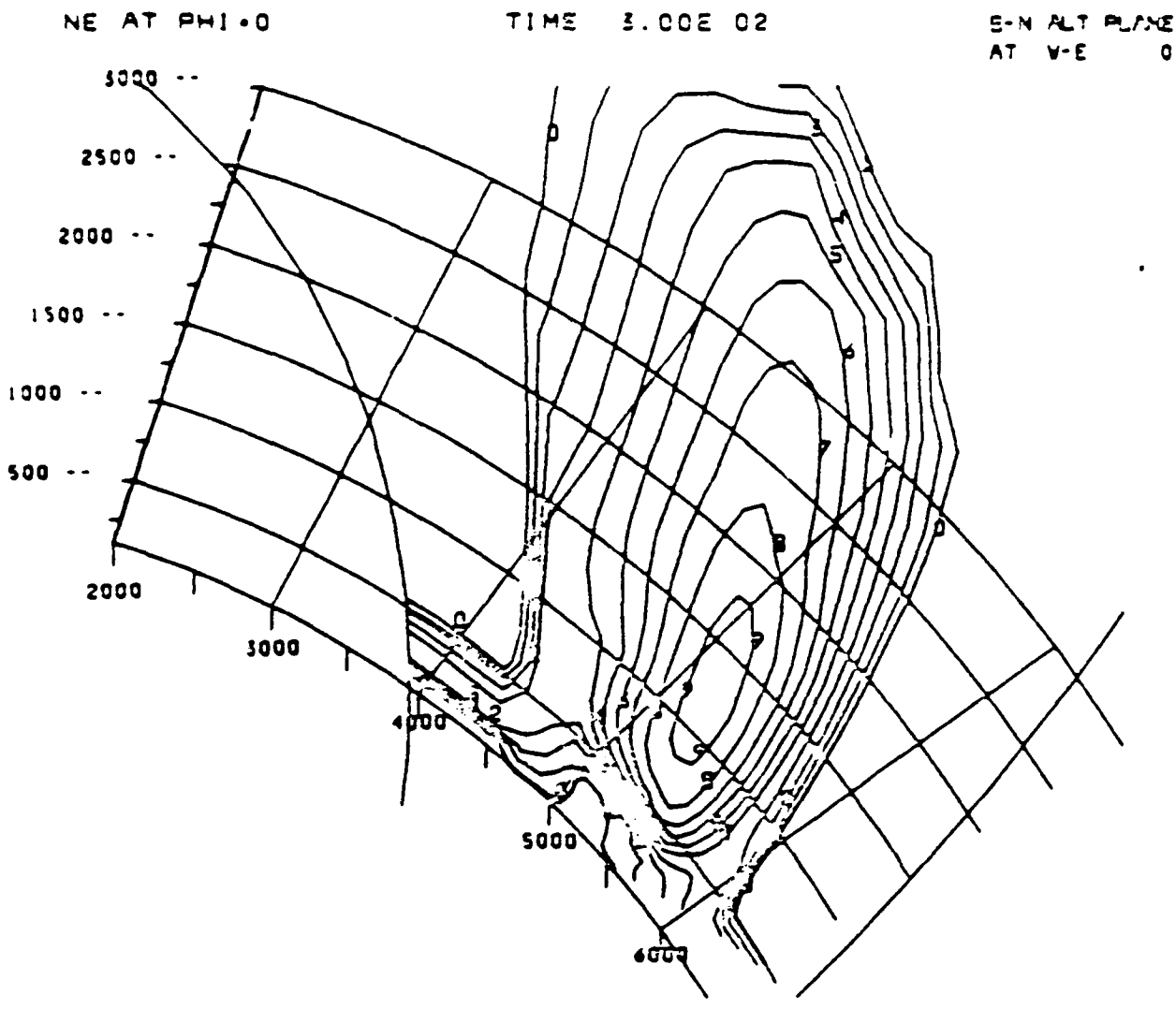

Figure 4. A contour plot of initial condition electron densities at 300 seconds on the northern conjugate central, meridion plane. Contour levels in electrons cm^{-3} are shown at the bottom of the graph.

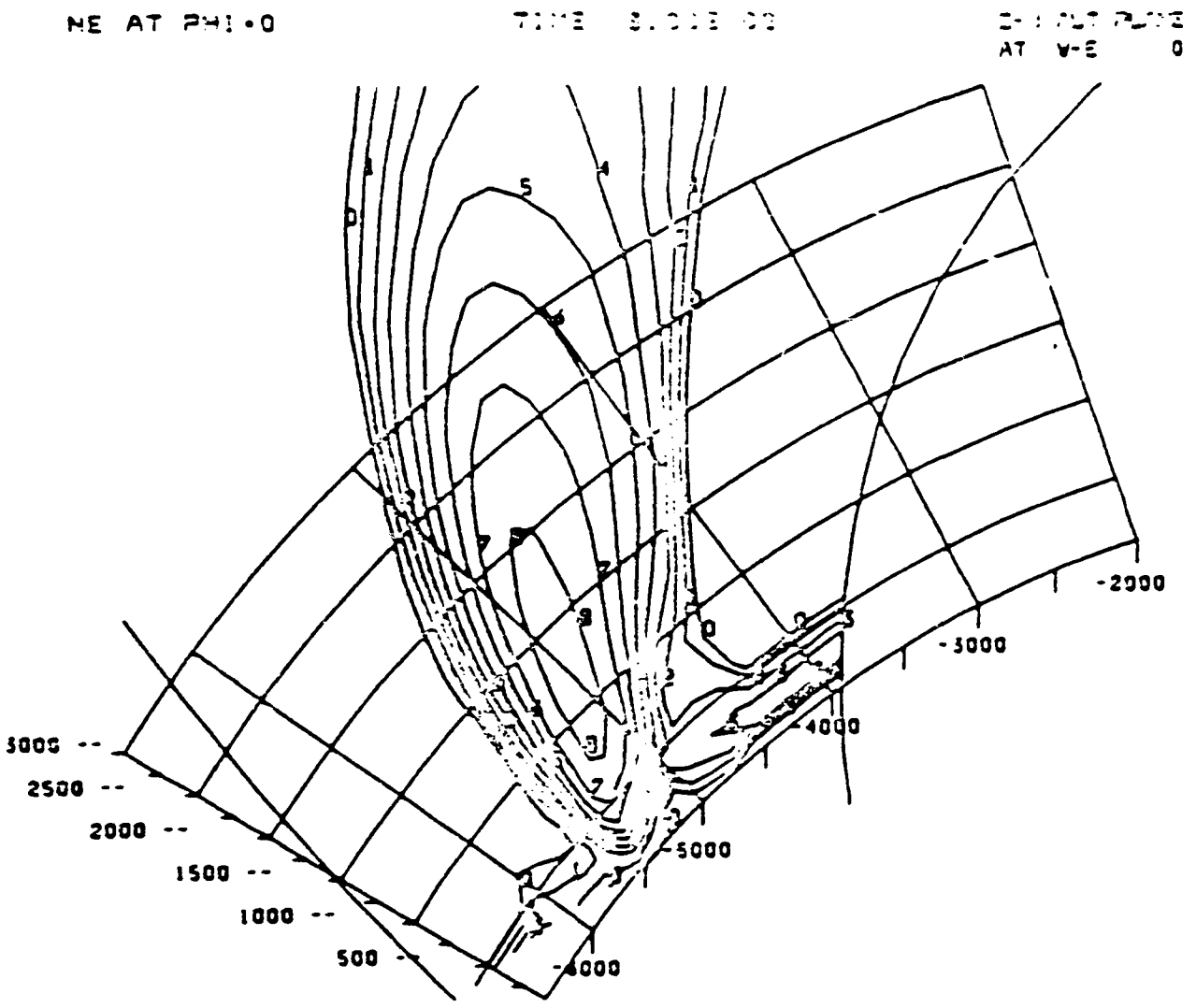

Figure 5. A contour plot of initial condition electron densities at 300 seconds on the southern conjugate central meridional plane. Contour levels in electrons cm^{-3} are shown at the bottom of the graph.

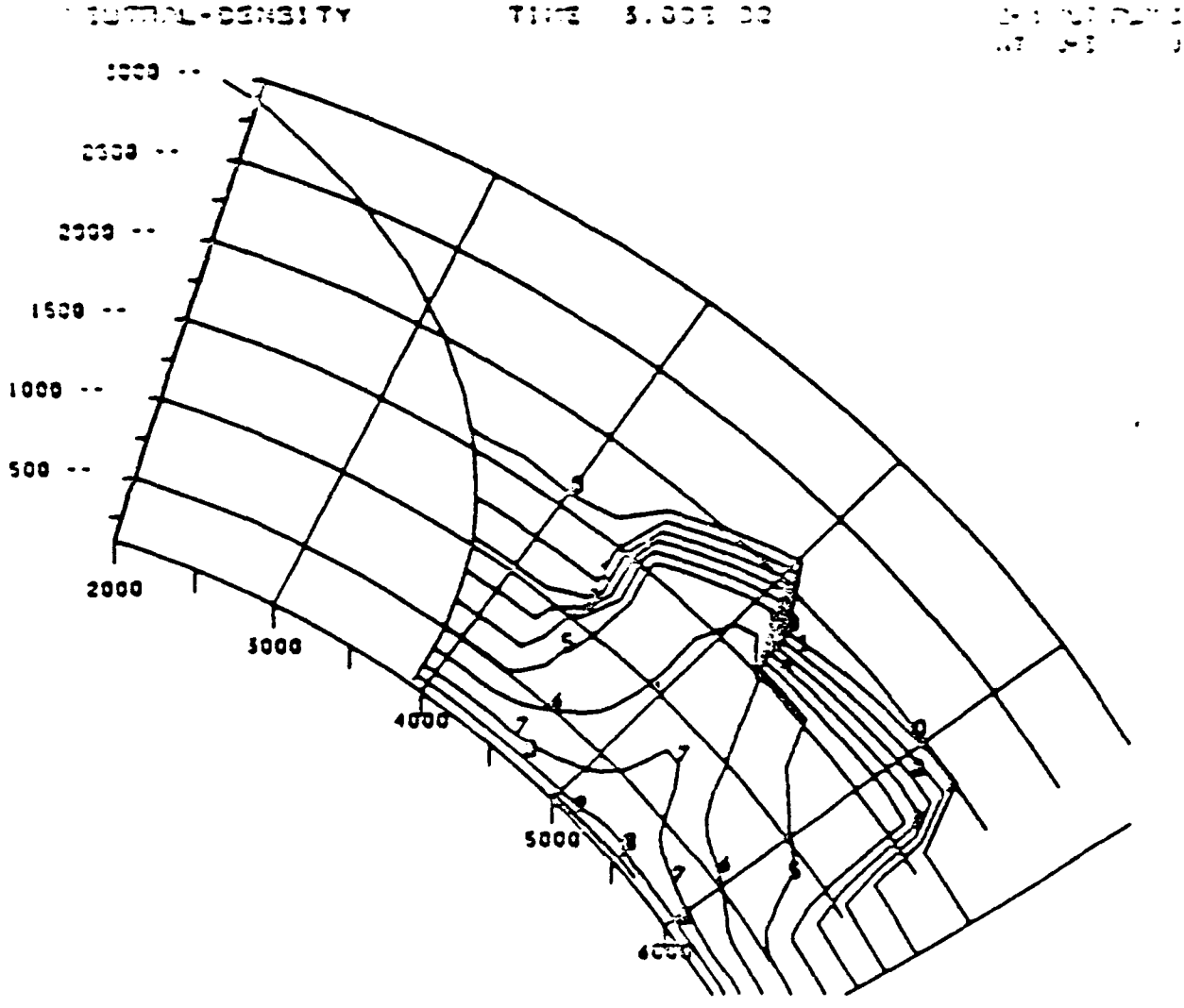

0• 1.0E-20 1• 1.0E-19 2• 1.0E-18 3• 1.0E-17 4• 1.0E-16

5• 1.0E-15 6• 1.0E-14 7• 1.0E-13 8• 1.0E-12 9• 1.0E-11 NLCY

Figure 6. A contour plot of initial conditions neutral atmospheric density at 300 seconds on the northern conjugate central meridion plane. Contour levels are shown in gauss cm^{-3} at the bottom of the graph. The sharp cutoff in atmospheric density above 1500 kilometers altitude is caused by the termination of the MICE/MELT neutral atmosphere numerical mesh.

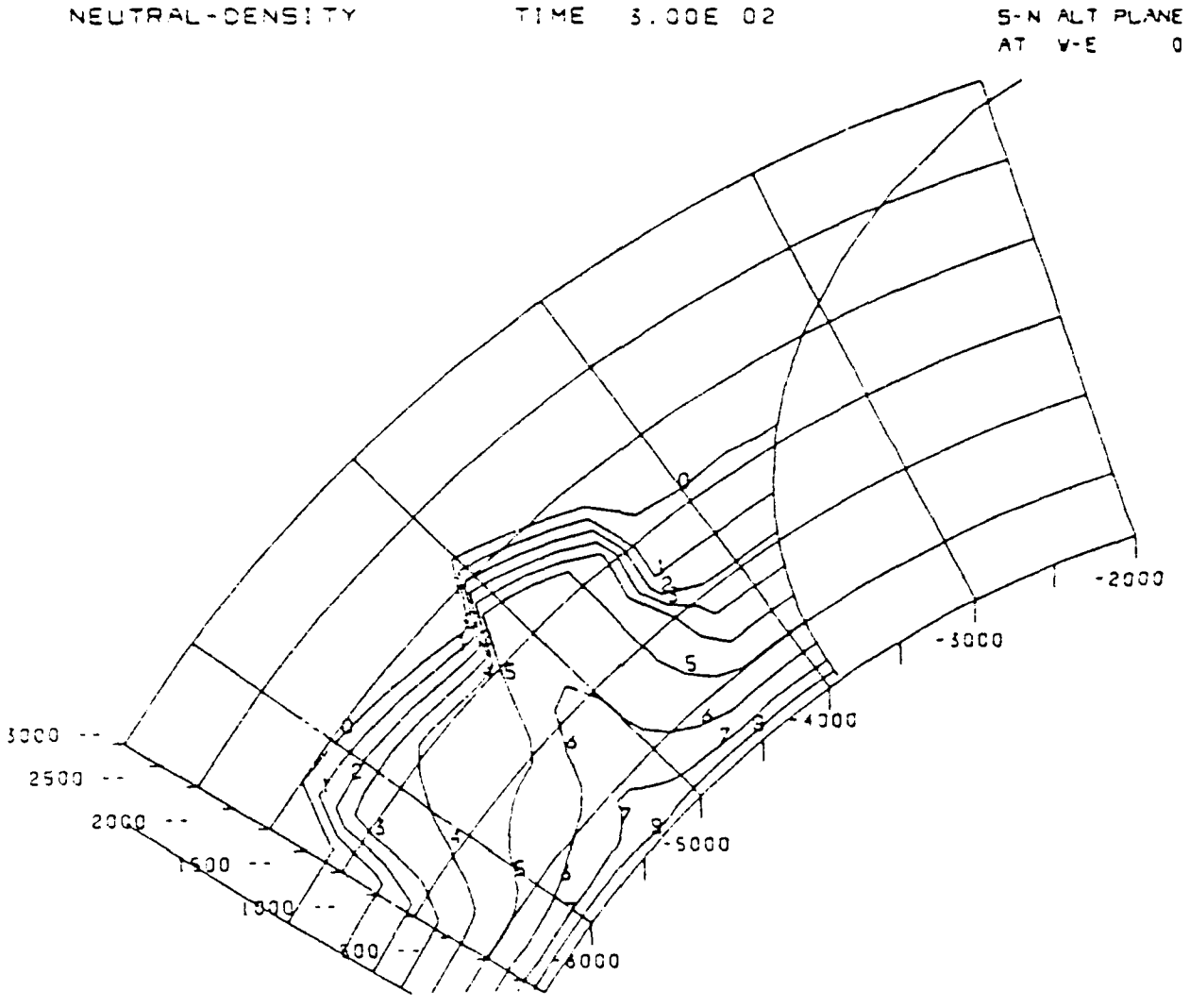

0• 1.0E-20 1• 1.0E-19 2• 1.0E-18 3• 1.0E-17 4• 1.0E-16

5• 1.0E-15 6• 1.0E-14 7• 1.0E-13 8• 1.0E-12 NLCY

Figure 7. A contour plot of the initial condition neutral atmospheric density at 300 seconds on the southern conjugate central meridion plane. Contour levels are shown in gauss cm^{-3} at the bottom of the graph.

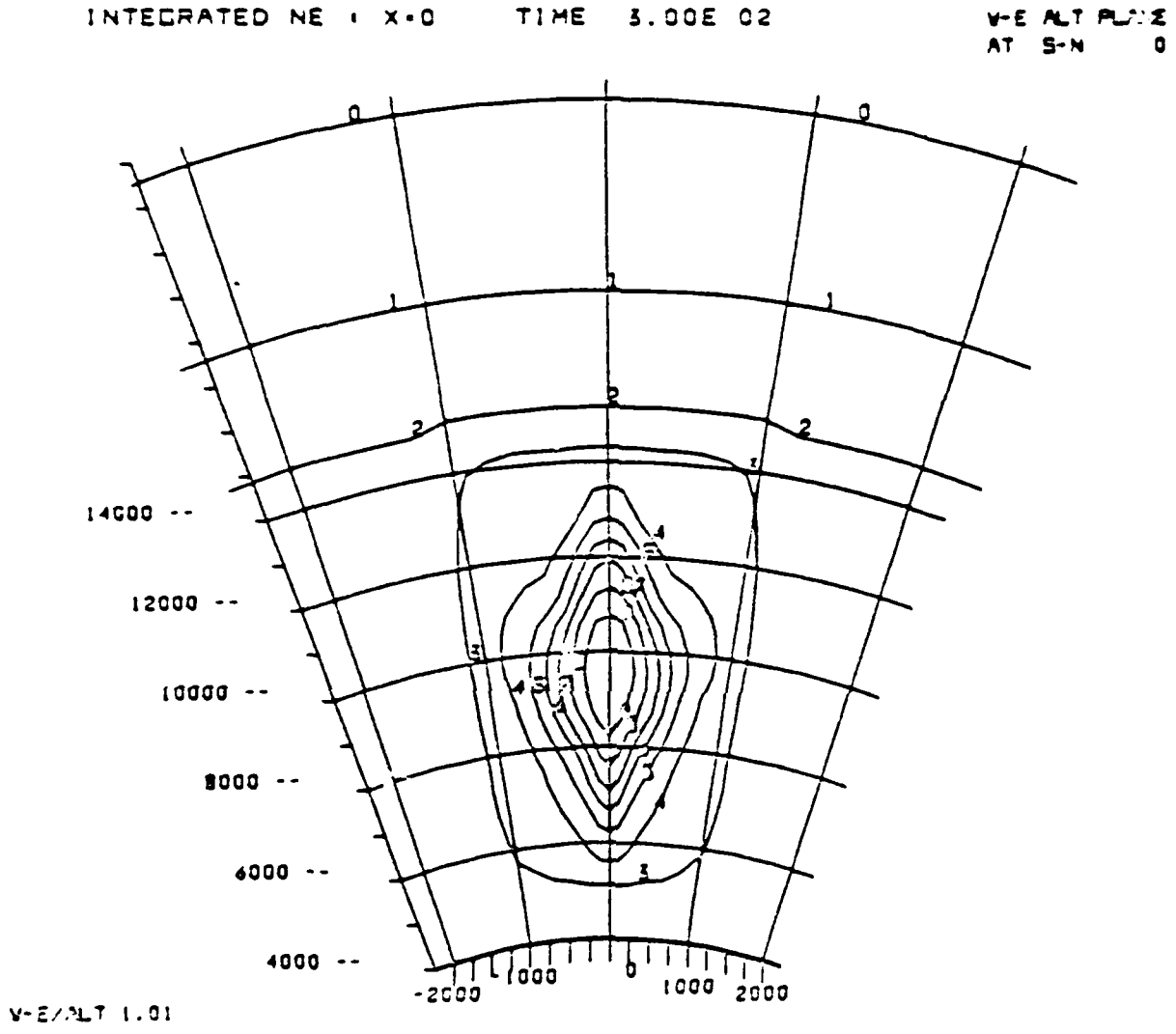

Figure 8. A contour plot of the field line integrated electron density at 300 seconds on the geomagnetic equatorial plane. Contour levels, shown at the bottom of the plot, are in electrons cm^{-2}. The vertical scale is kilometer altitude and the horizontal scale is kilometers longitude at the earth's surface.

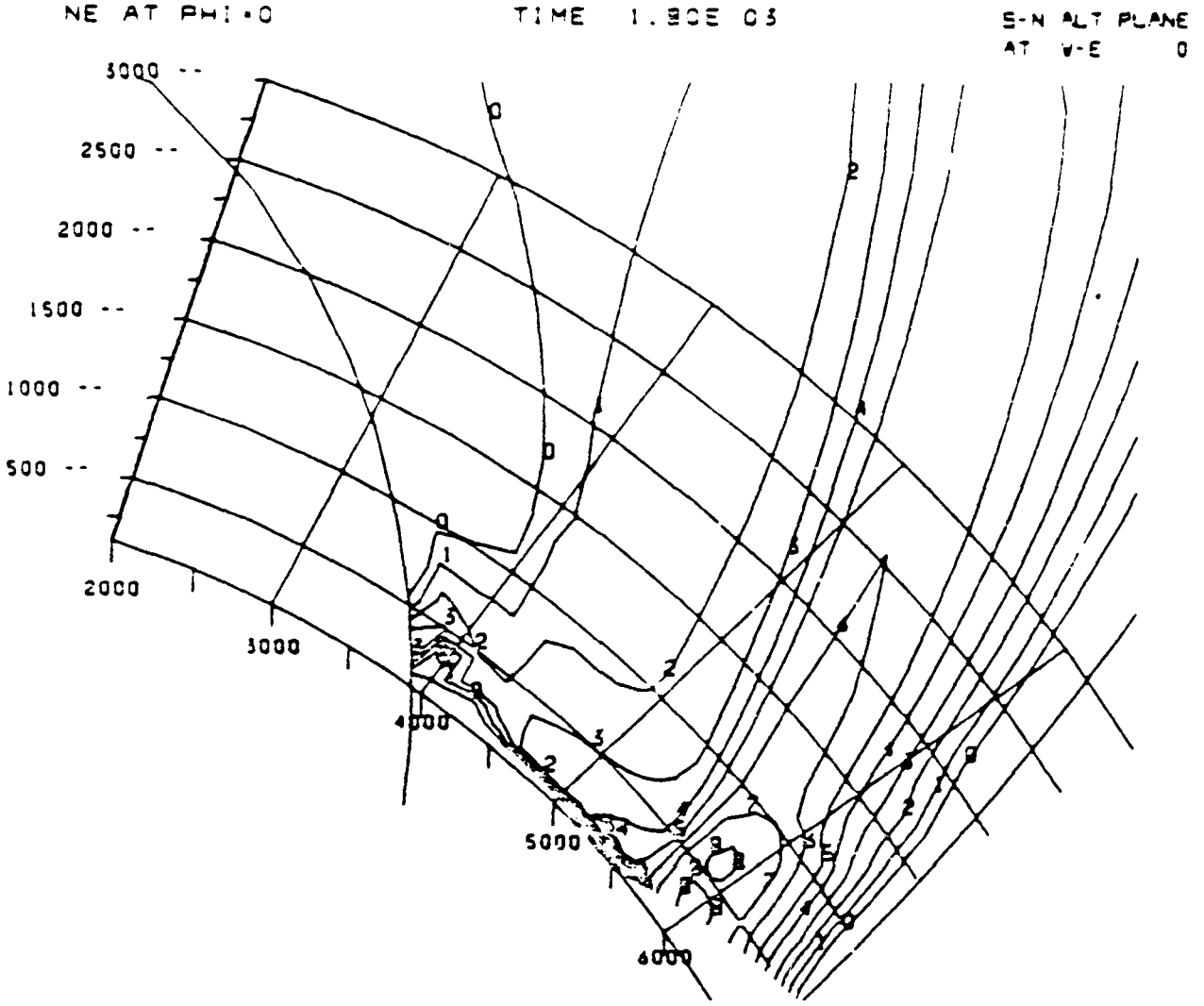

Figure 9. A contour plot of the electron density in the northern conjugate central meridion plane at 1800 seconds from the DEMAG simulation. Note the northward motion of the plasma plume relative to its location at 300 seconds in Figure 4. The plasma densities have also fallen by about a factor of 3 at the lower altitudes.

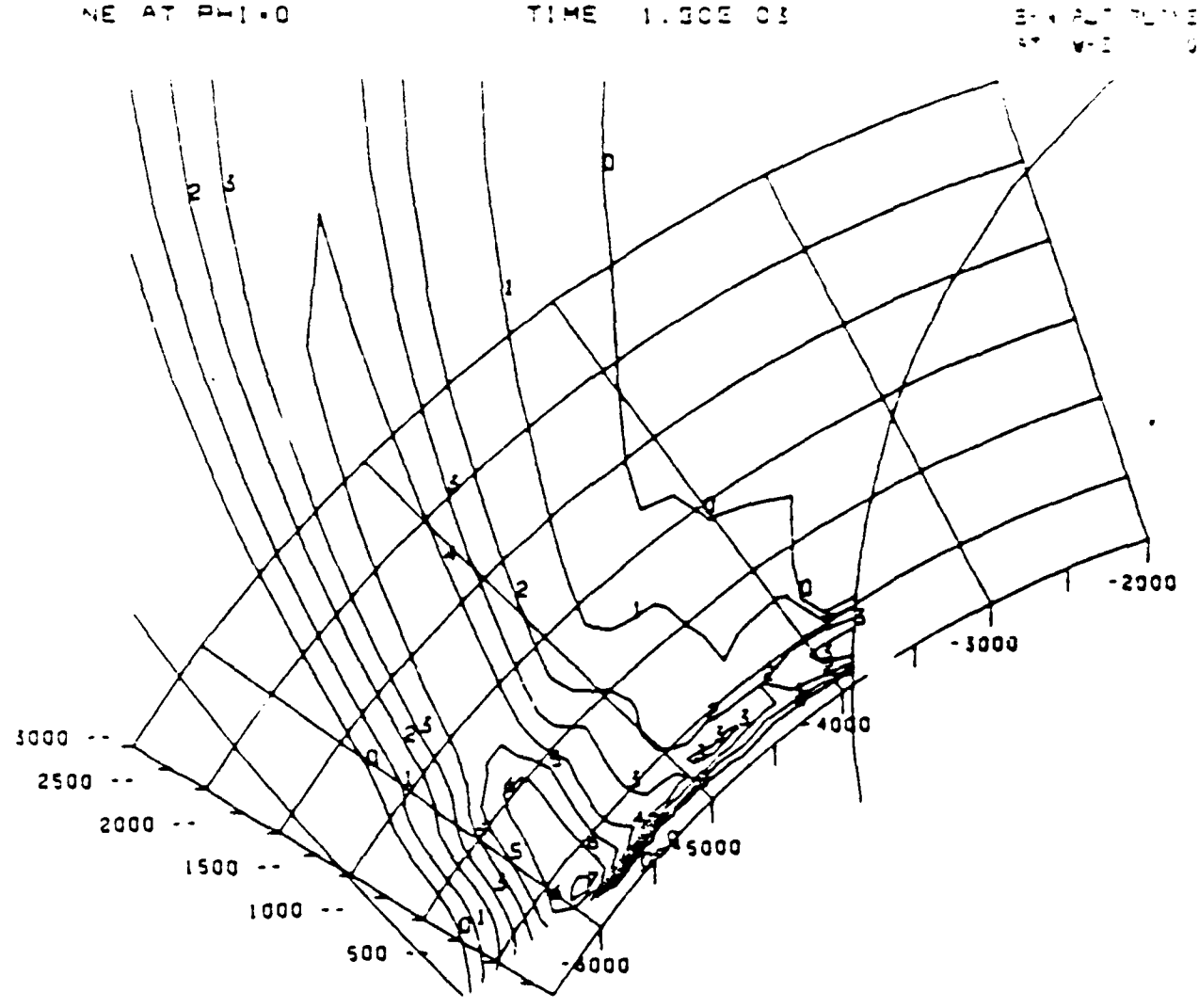

Figure 10. A contour plot of the electron density in the southern conjugate central meridion plane at 1800 seconds from the OEMAG simulation. We again notice the poleward motion and the reduction of plasma density at low altitudes.

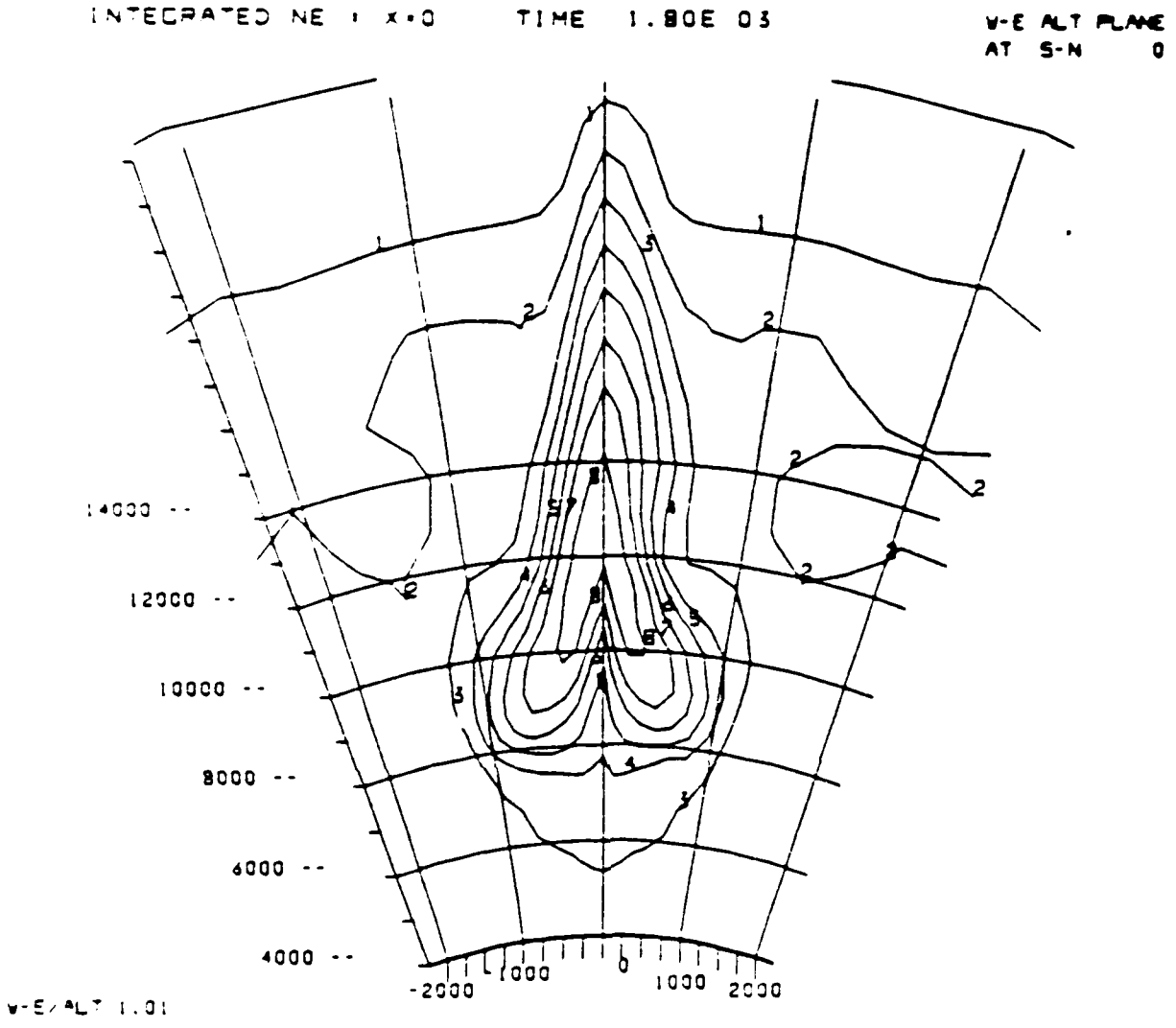

Figure 11. A contour plot of the field line integrated electron density in the geomagnetic equatorial plane at 1800 seconds from the DEMAG simulation. In comparing this plot to Figure 8 we note that the central portion of the plasma plume has moved dramatically upward and poleward. However, the eastward and westward portions of the plume have moved very little.

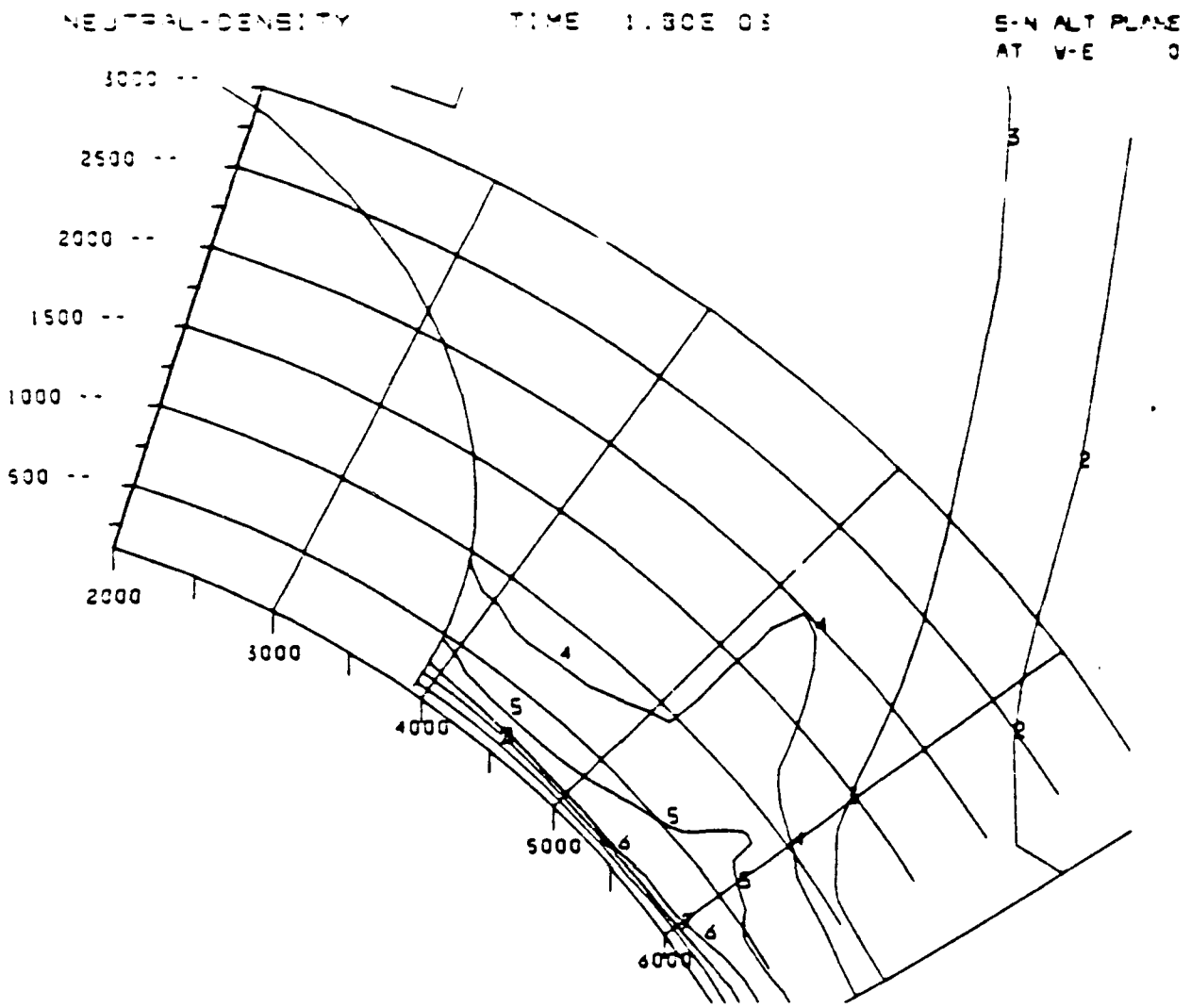

Figure 12. A contour plot of the neutral atmospheric density in the northern conjugate central meridion plane at 1800 seconds from the DEMAG simulation. By this time the neutral atmospheric density has almost returned to its ambient values.

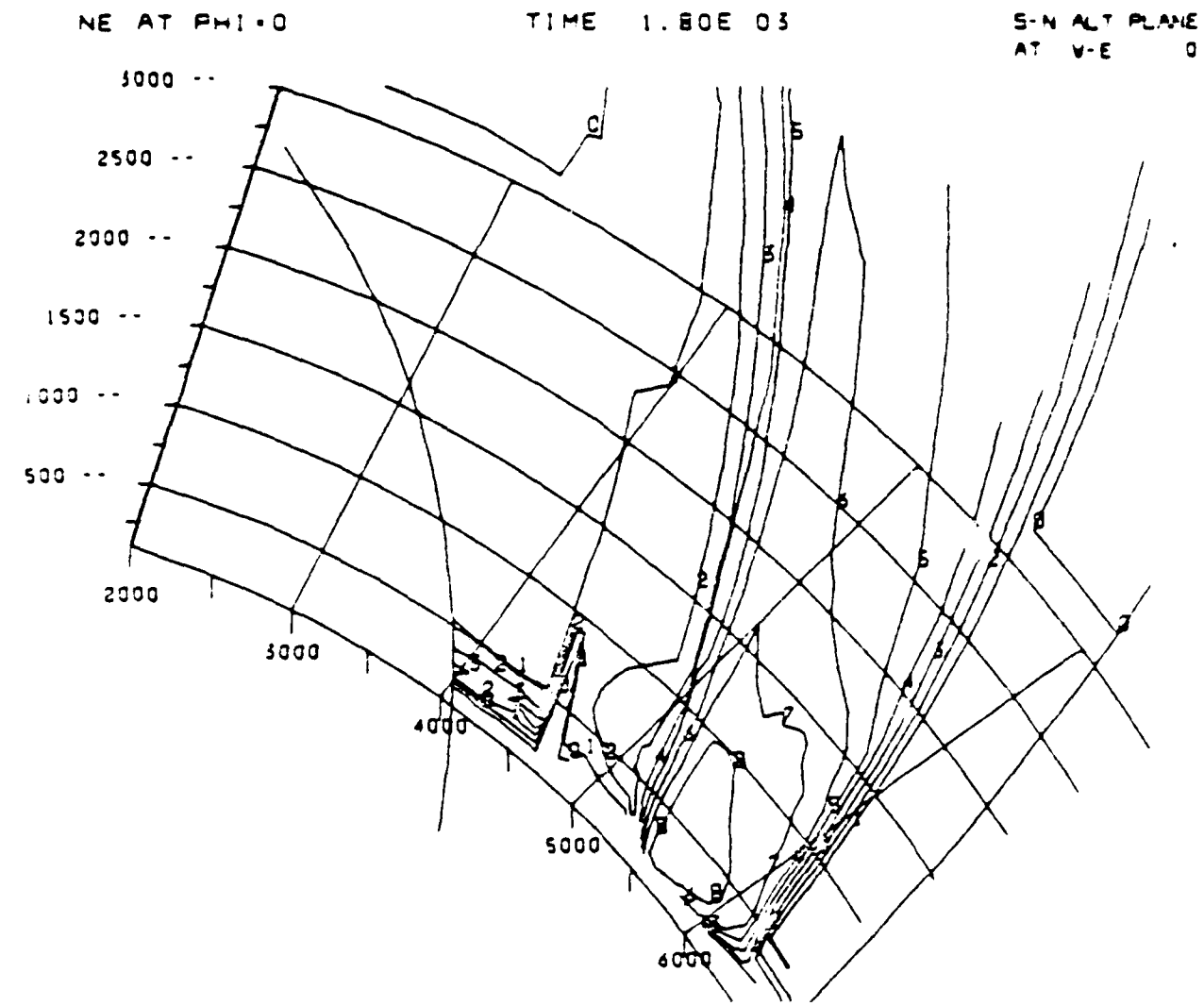

Figure 13. A contour plot of the electron density from the MELT simulation in the northern conjugate central meridion plane at 1800 seconds. These results are to be compared to the DEMAC results in Figure 9.

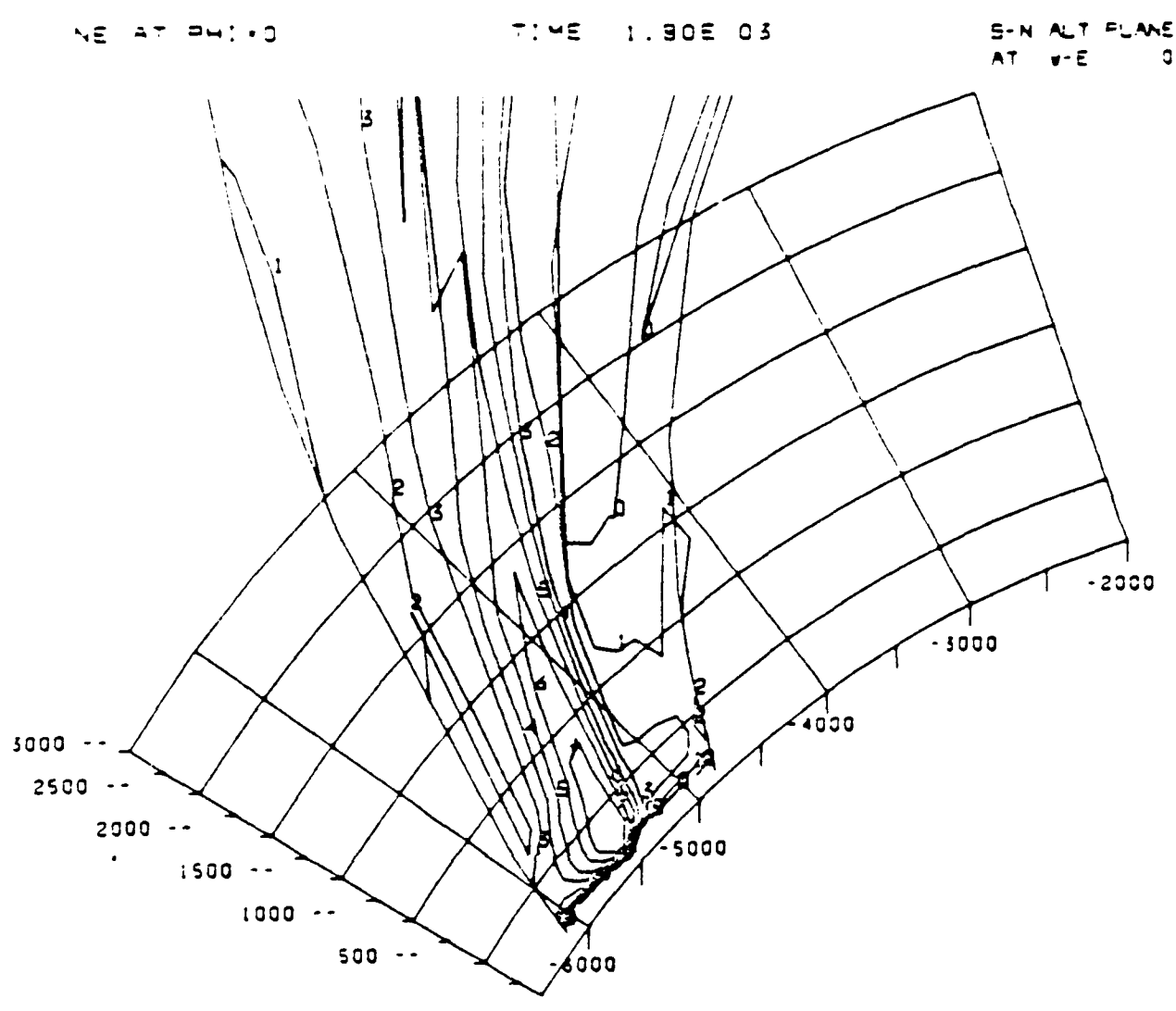

Figure 14. A contour plot of the electron density from the MELT simulation in the southern conjugate central meridion plane at 1800 seconds. These results are to be compared to the DEMAG results in Figure 10.

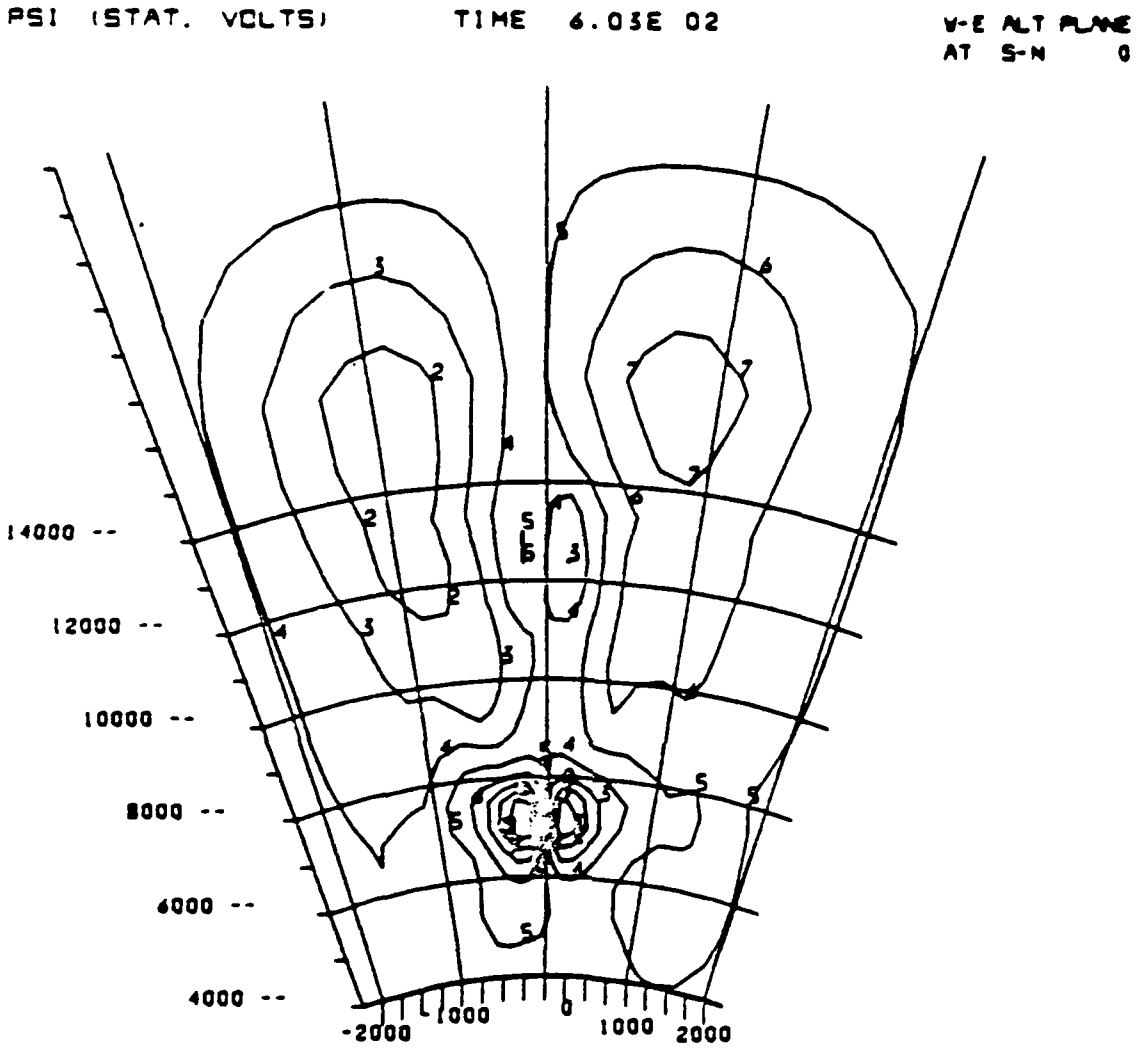

Figure 15. A contour plot of the electrostatic potential at 600 seconds for the DEMAG simulation shown on the geomagnetic equatorial plane. The contour levels are shown at the bottom of the diagram for the potential and are in stat volts. See text for a discussion of the results.

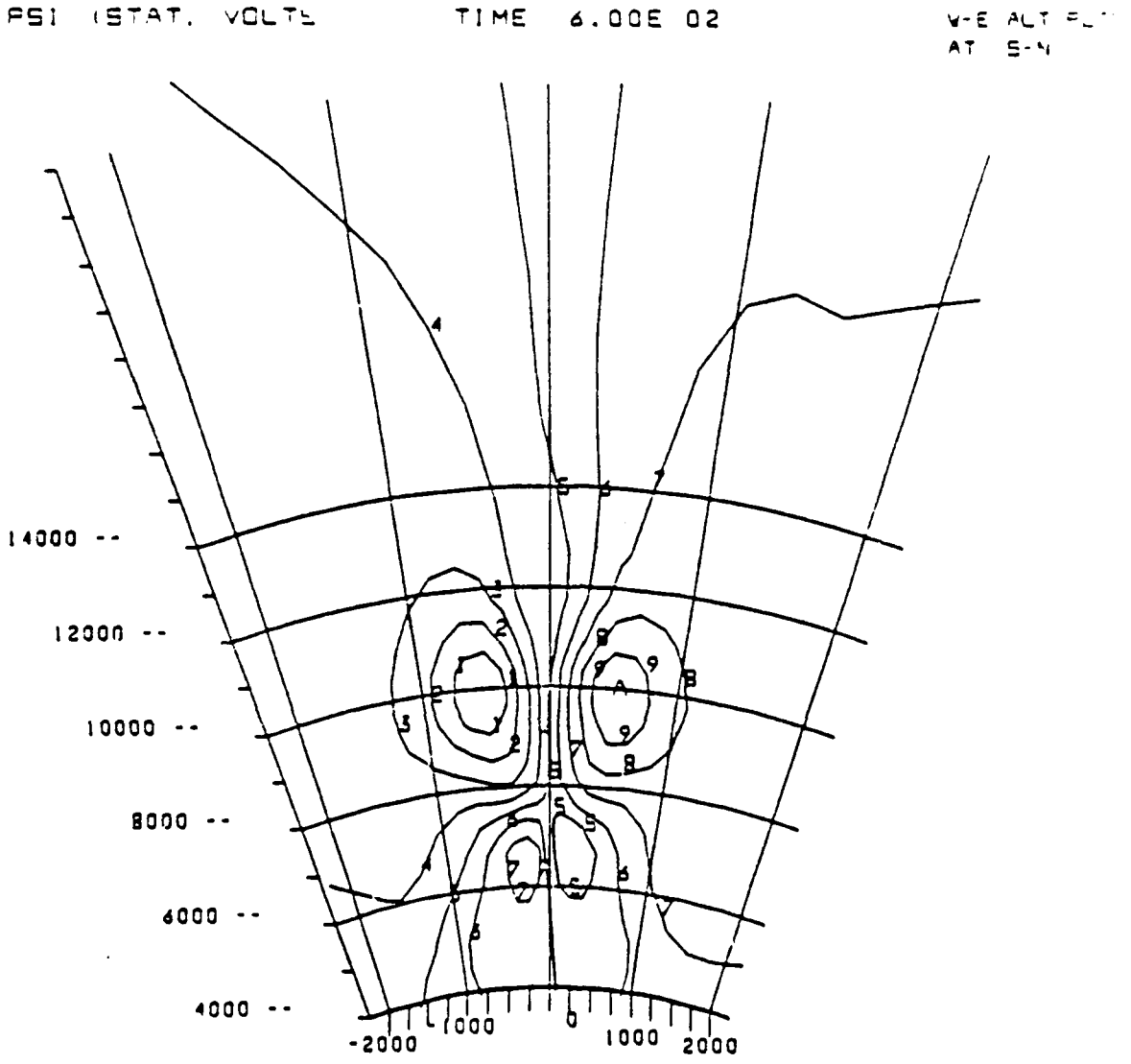

Figure 16. A contour plot of the electrostatic potential at 600 seconds for the MELT simulation shown on the geomagnetic equatorial plane. The contour levels are shown at the bottom of the diagram for the potential in stat volts.

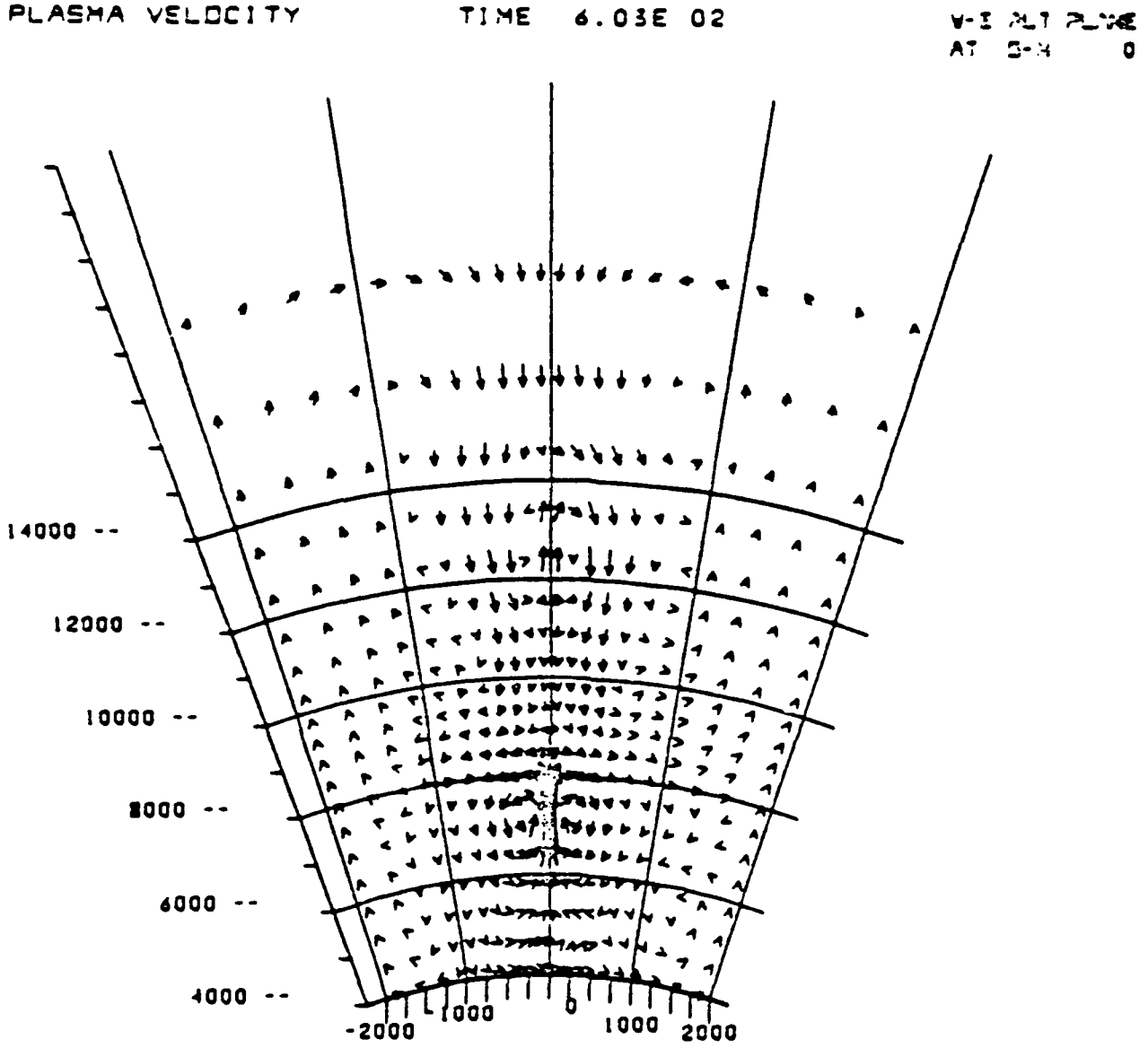

Figure 17. A vector plot of the velocity perpendicular to the geomagnetic field in the equatorial plane for the DEMAG simulations at 600 seconds. The velocity scale is shown at the bottom in cm sec^{-1}. See text for a discussion.

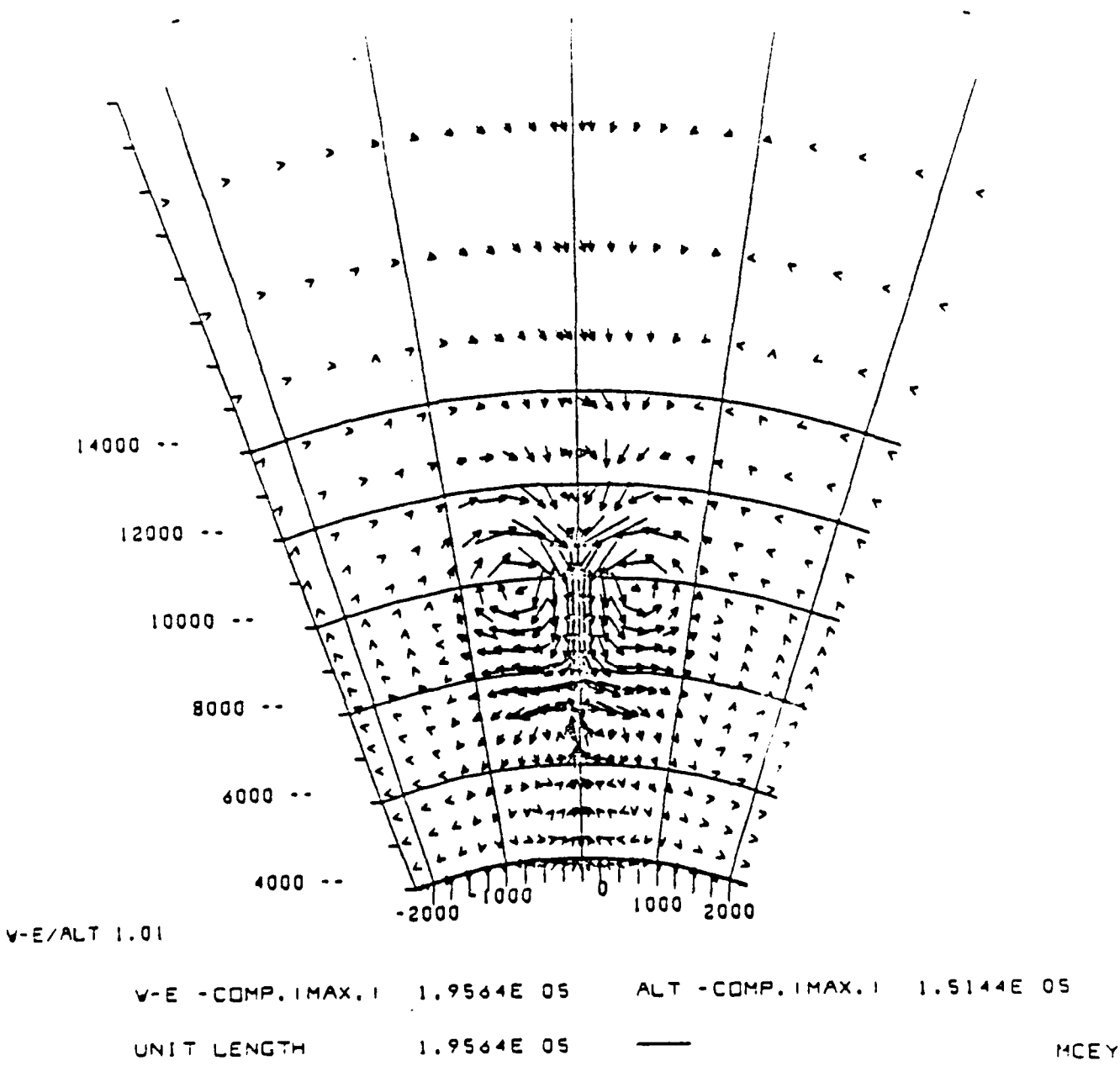

Figure 18. A vector plot of the velocity perpendicular to the geomagnetic field in the equatorial plane for the MELT simulation at 600 seconds. The velocity scale is shown in cm sec^{-1}.

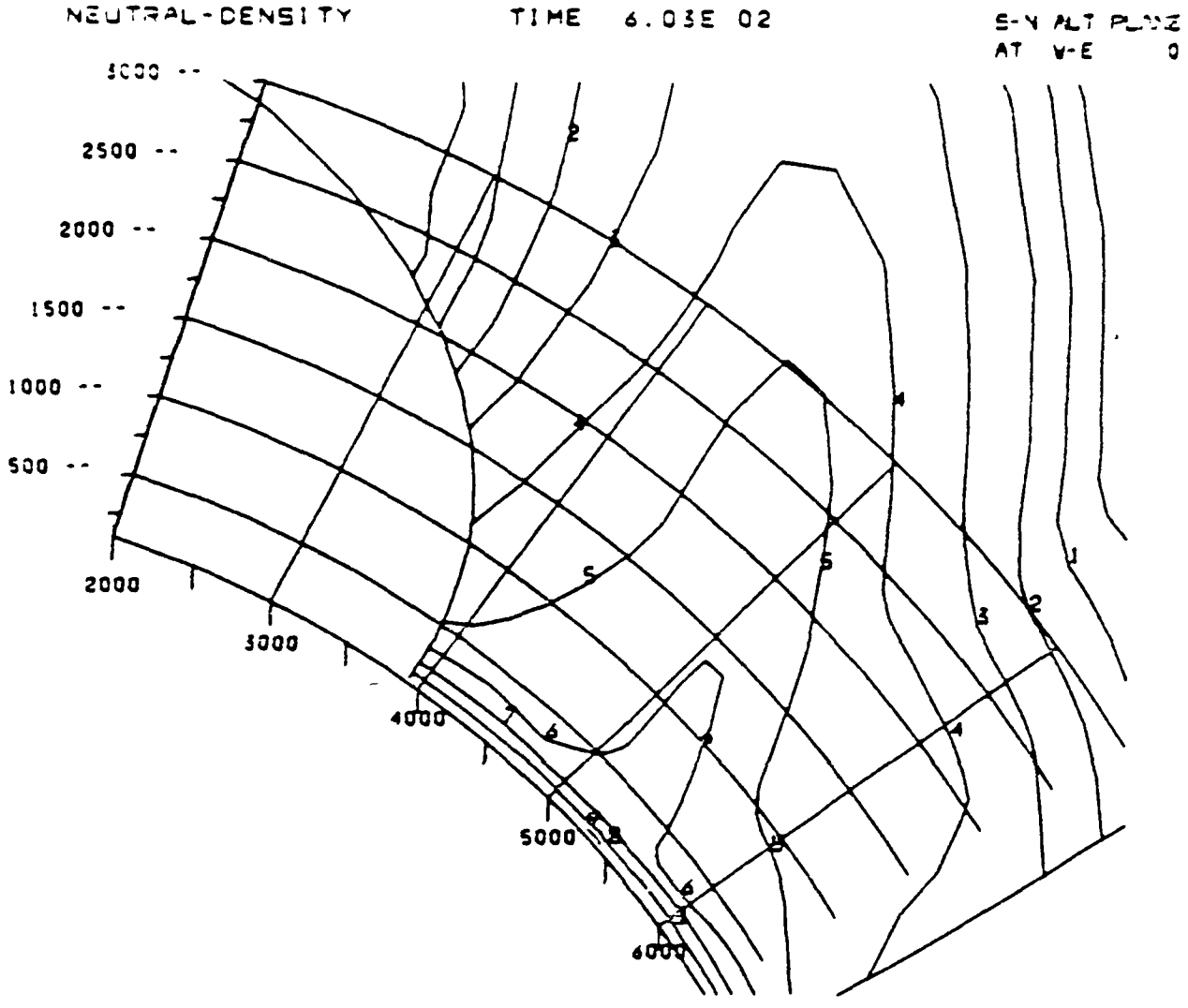

Figure 19. A contour plot of the neutral atmospheric density in the northern conjugate central meridion plane for the DEMAG simulation at 600 secs. Notice the high densities above 1500 km altitude which are not considered in the MELT simulation.

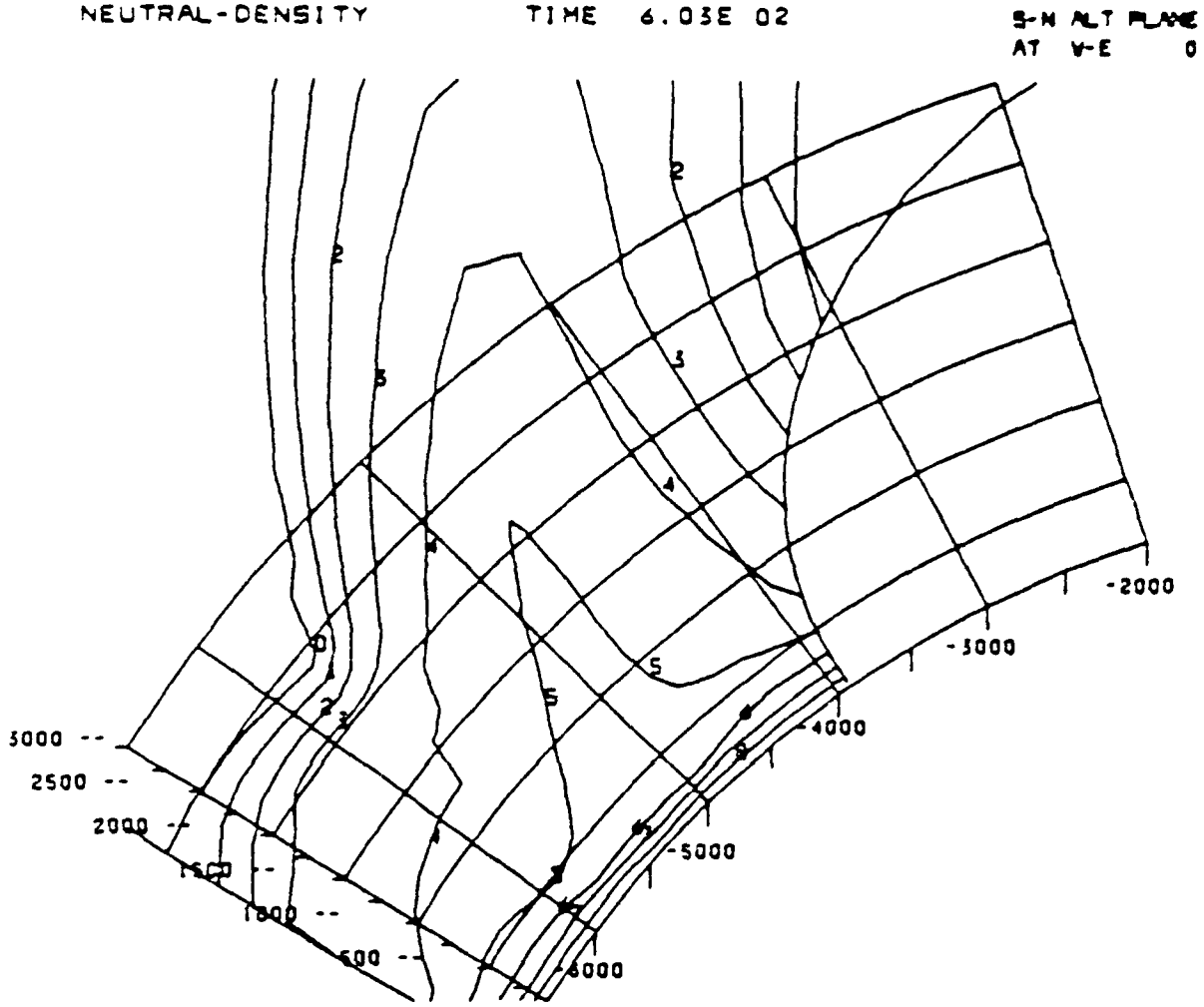

0• 1.0E-20 1• 1.0E-19 2• 1.0E-18 3• 1.0E-17 4• 1.0E-16

5• 1.0E-15 6• 1.0E-14 7• 1.0E-13 8• 1.0E-12 NLCY

Figure 20. A contour plot of the neutral atmospheric density in the southern conjugate central meridion plane for the DEMAG simulation at 600 secs. Similar comments to those for Figure 19 apply.

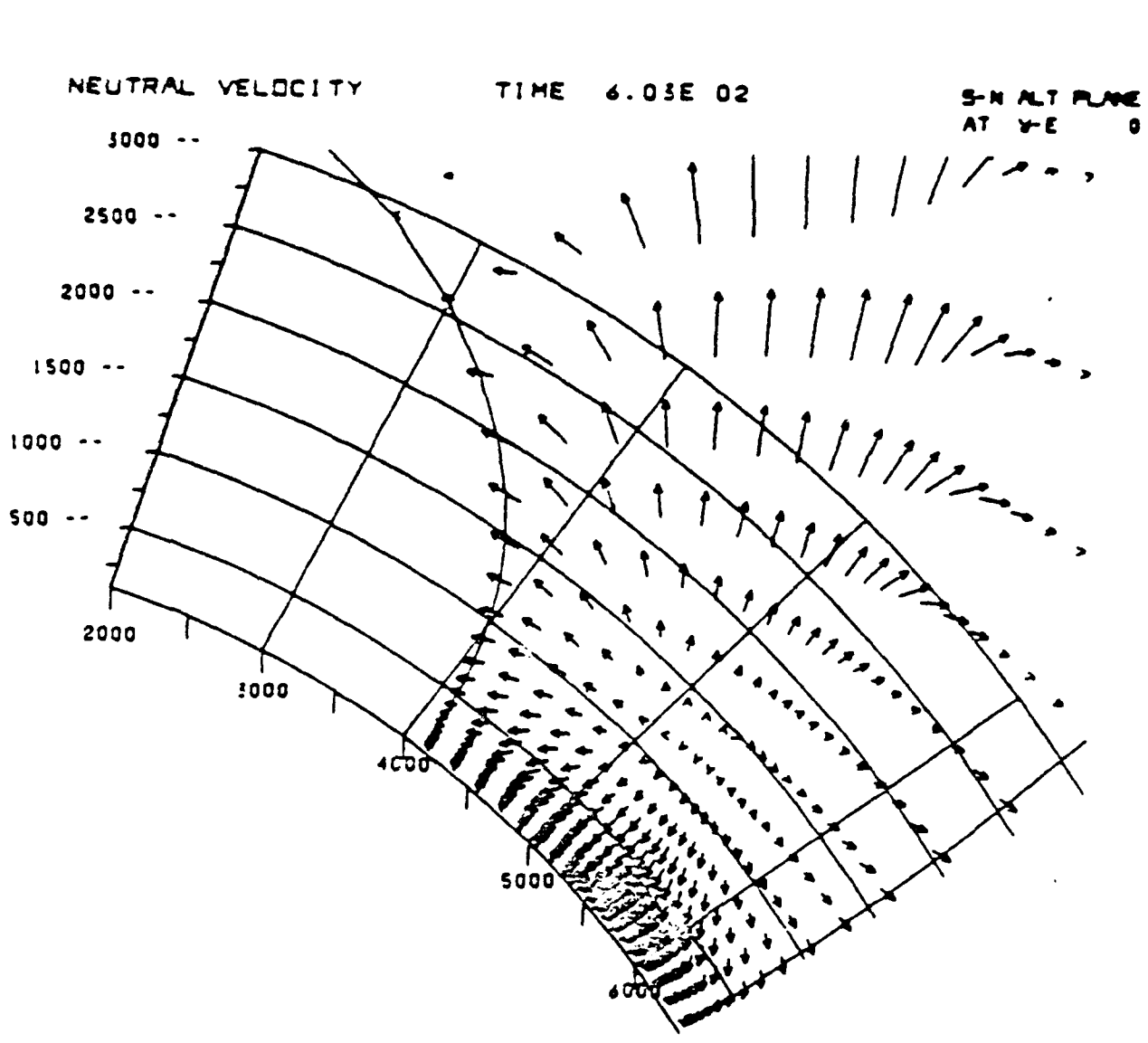

Figure 21. A vector plot of neutral velocity for the DEMAG simulation in the northern conjugate central meridion plane at 600 seconds. Notice the large upward and poleward, relative to the geomagnetic field, velocities at altitudes above 1500 kilometers.

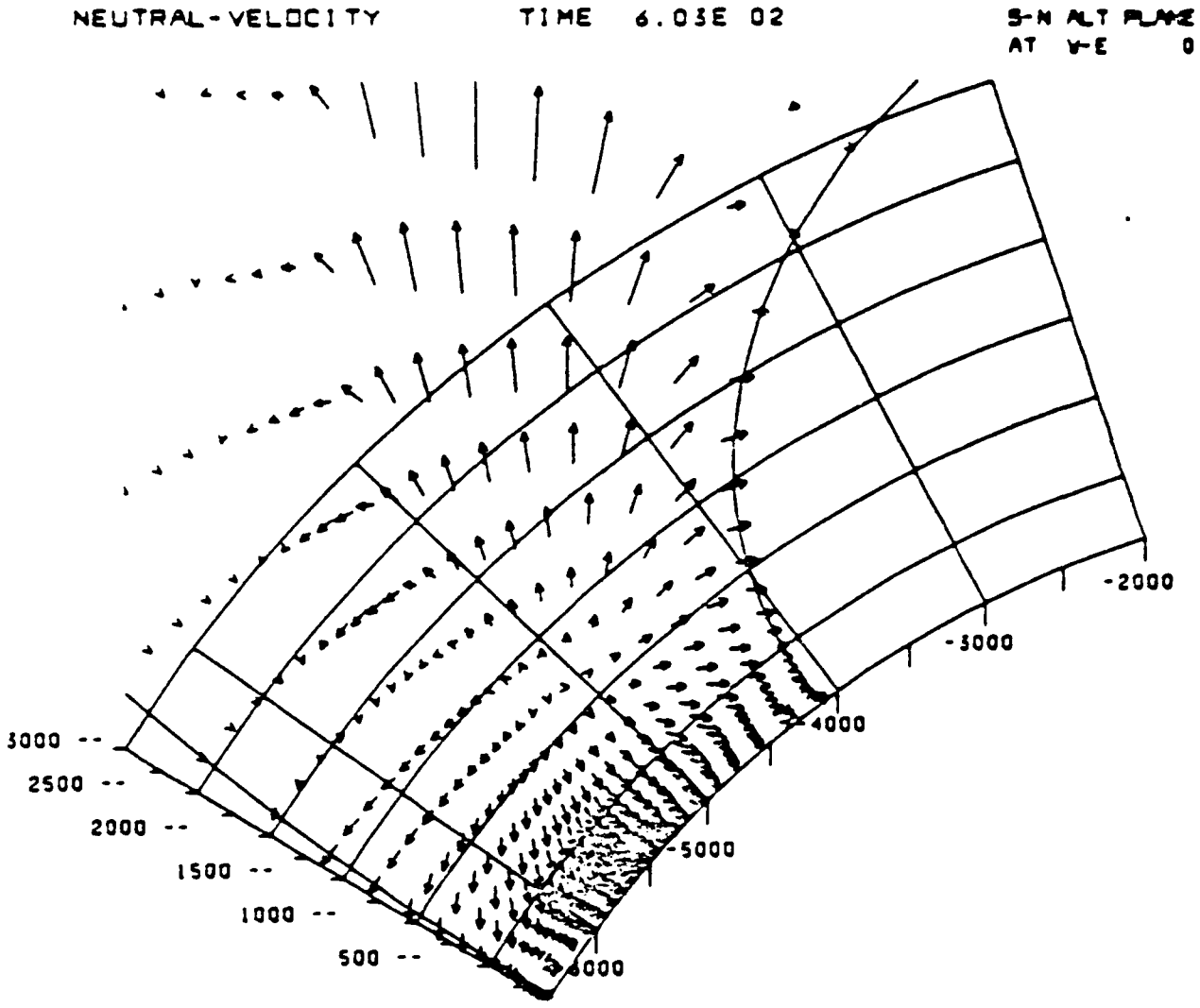

Figure 22. A vector plot of neutral velocity for the DEMAG simulation in the southern conjugate central meridion plane at 600 seconds. Comments similar to those for Figure 21 apply.

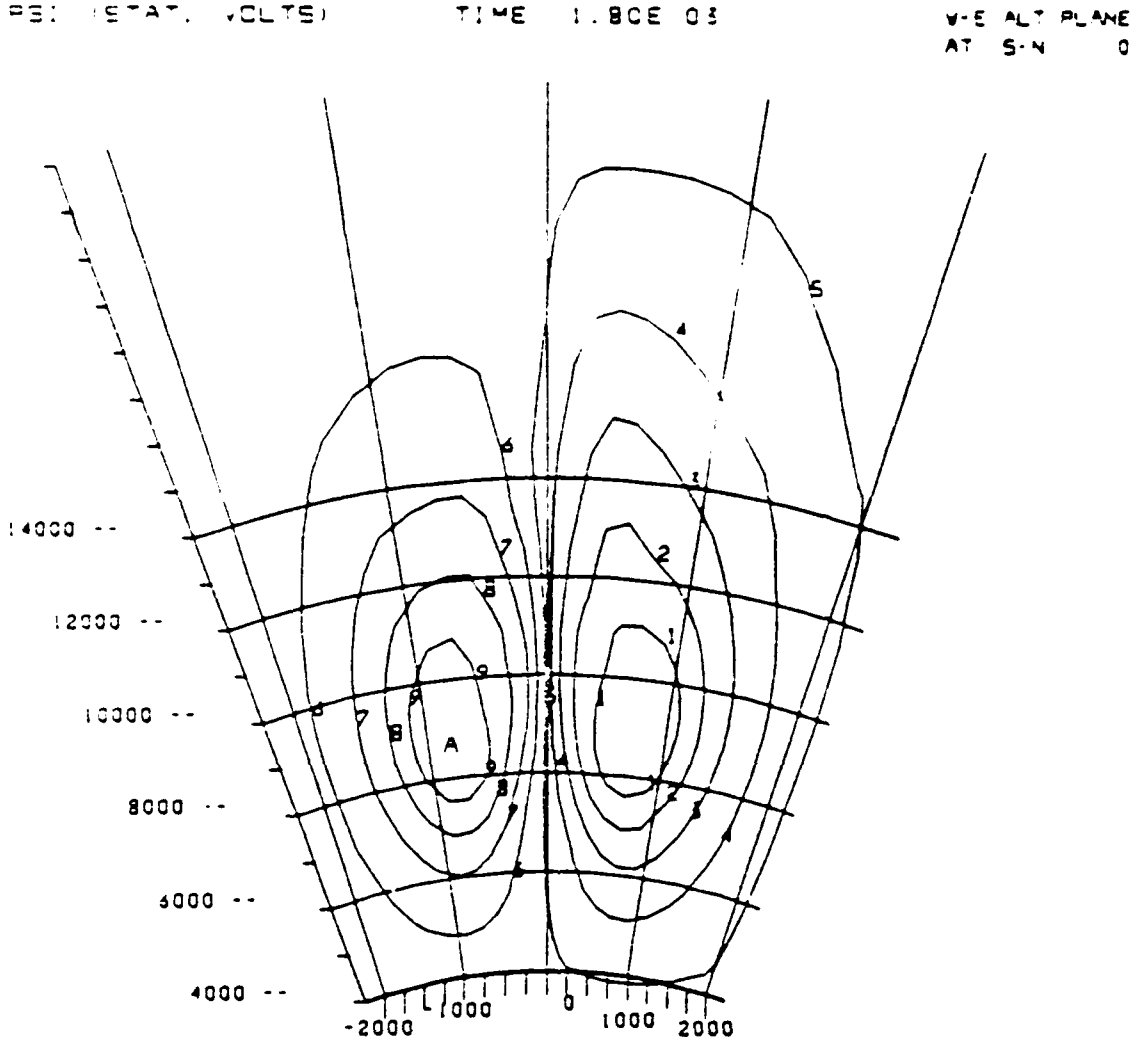

Figure 23. A contour plot of the electrostatic potential for the DEMAG simulation in the geomagnetic equatorial plane at 1800 seconds. Refer to the text for discussion.

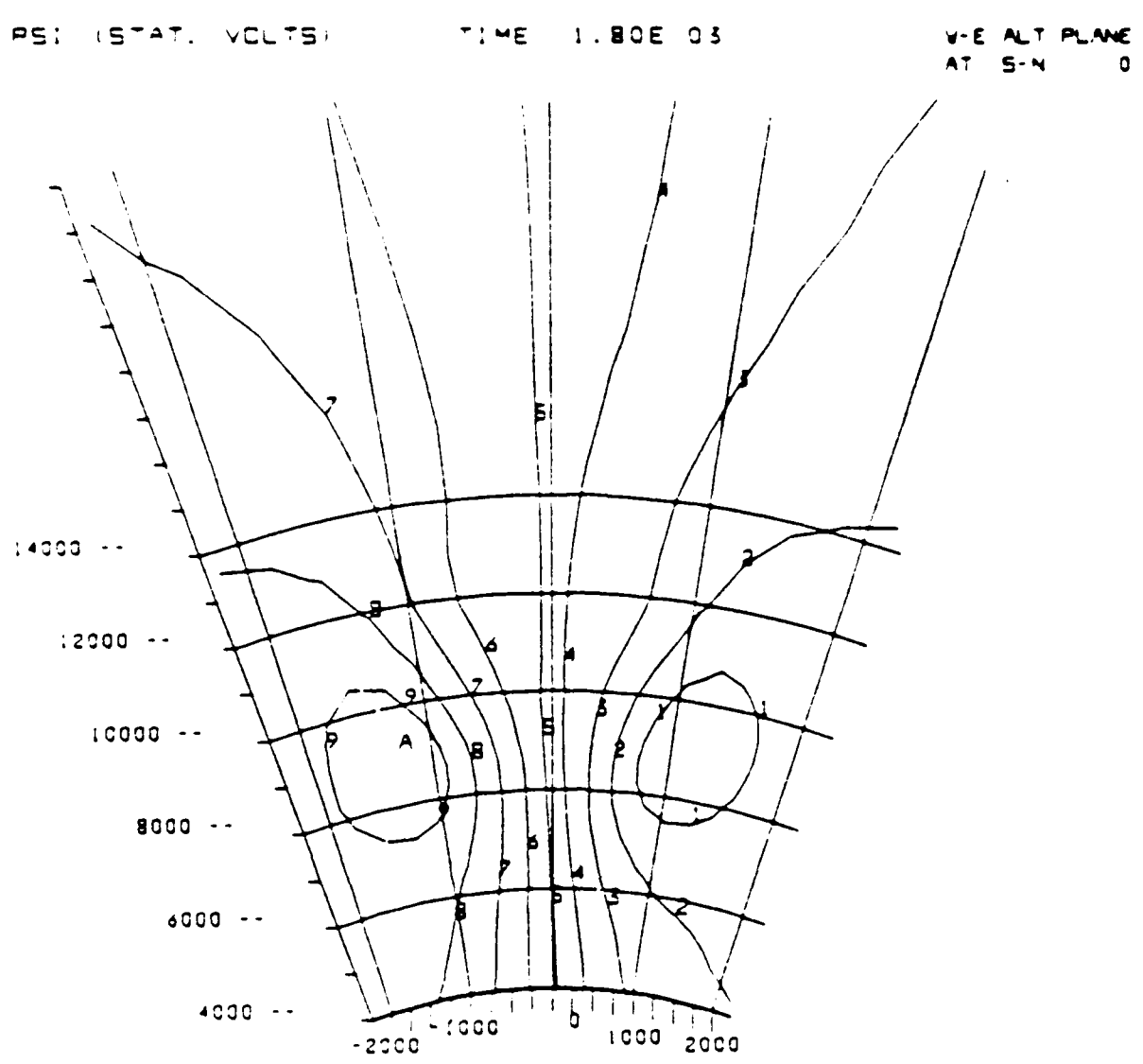

Figure 24. A contour plot of the electrostatic potential for the MELT simulation in the geomagnetic equatorial plane at 1800 seconds.

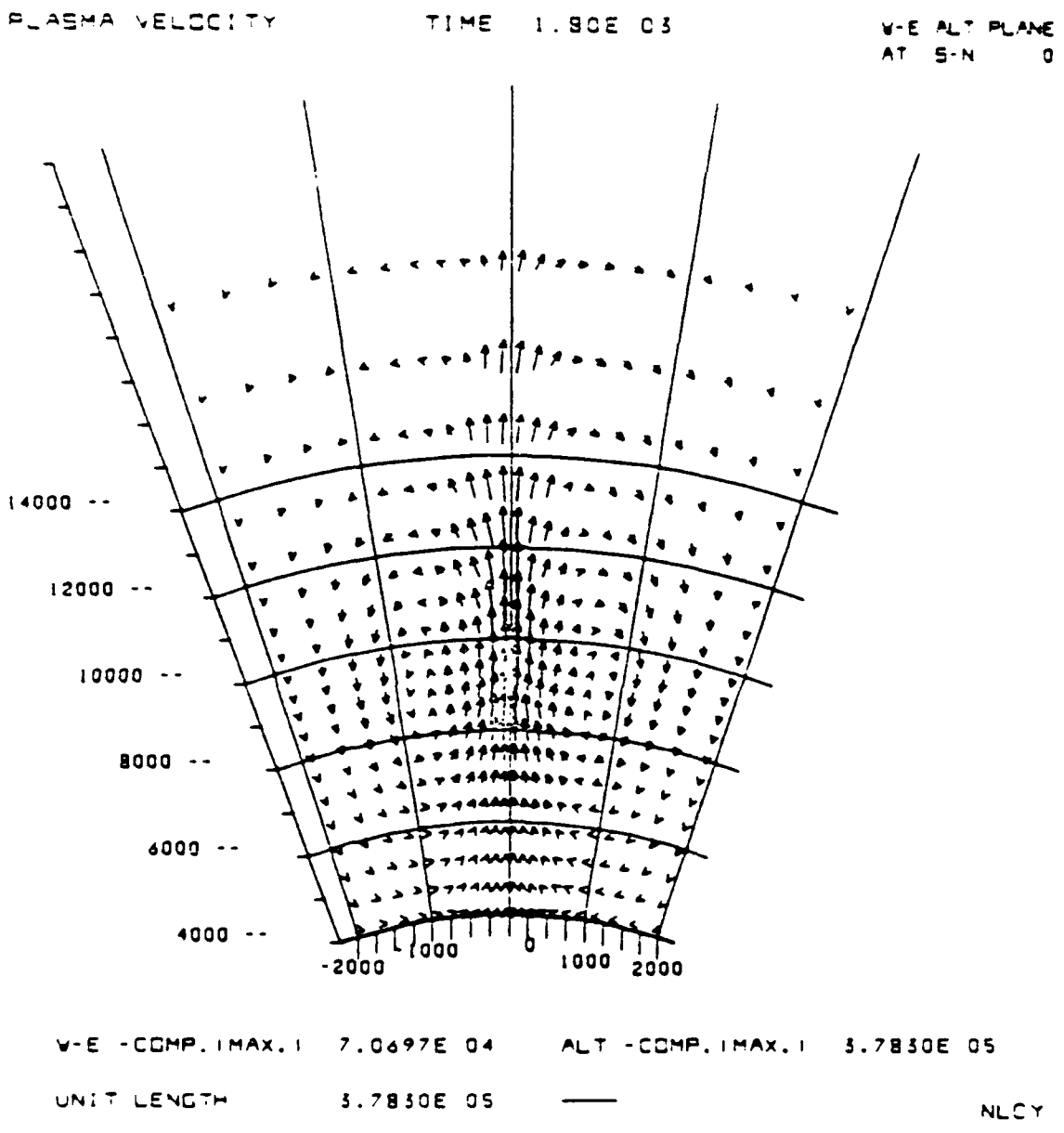

Figure 25. A vector plot of perpendicular velocities in the geomagnetic equatorial plane for 1800 seconds from the DEMAG simulation. Refer to the text for discussion.

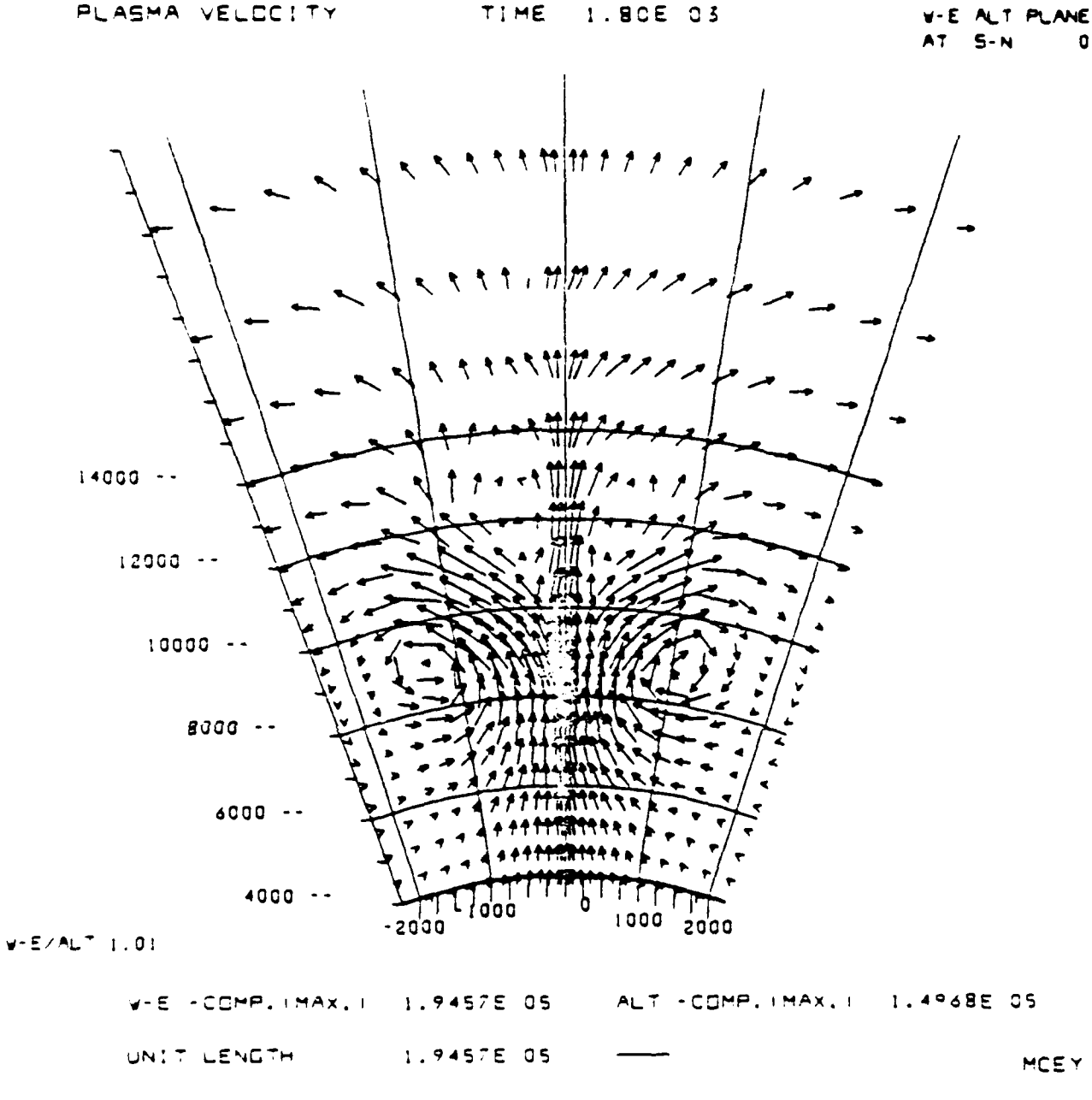

Figure 26. A vector plot of perpendicular velocities in the geomagnetic equatorial plane for 1800 seconds from the MELT simulations.

References

Hain, K. and J. Fedder, "Electrostatic equations for large scale plasma simulation studies," NRL Memo Rept. 5385, 1984.

Kilb, R.W., "Striation Formation," in Physics of High Altitude Nuclear Burst Effects, DNA 4501F, 1977.

Longmire, C.L. and R.W. Kilb, "Plasma Physics," in Physics of High Altitude Nuclear Burst Effects, DNA 4501F, 1977.

DISTRIBUTION LIST

DEPARTMENT OF DEFENSE

ASSISTANT SECRETARY OF DEFENSE
COMM, CMD, CONT 7 INTELL
WASHINGTON, D.C. 20301

DIRECTOR
COMMAND CONTROL TECHNICAL CENTER
PENTAGON RM BE 685
WASHINGTON, D.C. 20301
01CY ATTN C-650
01CY ATTN C-312 R. MASON

DIRECTOR
DEFENSE ADVANCED RSCH PROJ AGENCY
ARCHITECT BUILDING
1400 WILSON BLVD.
ARLINGTON, VA. 22209
01CY ATTN NUCLEAR
MONITORING RESEARCH
01CY ATTN STRATEGIC TECH OFFICE

DEFENSE COMMUNICATION ENGINEER CENTER
1860 WIEHLE AVENUE
RESTON, VA. 22090
01CY ATTN CODE R410
01CY ATTN CODE R812

DEFENSE TECHNICAL INFORMATION CENTER
CAMERON STATION
ALEXANDRIA, VA. 22314
02CY

DIRECTOR
DEFENSE NUCLEAR AGENCY
WASHINGTON, D.C. 20305
01CY ATTN STVL
04CY ATTN TITL
01CY ATTN DDST
03CY ATTN RAAE

COMMANDER
FIELD COMMAND
DEFENSE NUCLEAR AGENCY
KIRTLAND, AFB, NM 87115
01CY ATTN FCPR

DEFENSE NUCLEAR AGENCY
SAO/DNA
BUILDING 20676
KIRTLAND AFB, NM 87115
01CY D.C. THORNBURG

DIRECTOR
INTERSERVICE NUCLEAR WEAPONS SCHOOL
KIRTLAND AFB, NM 87115
01CY ATTN DOCUMENT CONTROL

JOINT CHIEFS OF STAFF
WASHINGTON, D.C. 20301
01CY ATTN J-3 WWMCCS EVALUATION
OFFICE

DIRECTOR
JOINT STRAT TGT PLANNING STAFF
OFFUTT AFB
OMAHA, NB 68113
01CY ATTN JSTPS/JLKS
01CY ATTN JPST G. GOETZ

CHIEF
LIVERMORE DIVISION FLD COMMAND DNA
DEPARTMENT OF DEFENSE
LAWRENCE LIVERMORE LABORATORY
P.O. BOX 808
LIVERMORE, CA 94550
01CY ATTN FCPRL

COMMANDANT
NATO SCHOOL (SHAPE)
APO NEW YORK 09172
01CY ATTN U.S. DOCUMENTS OFFICER

UNDER SECY OF DEF FOR RSCH & ENGRG
DEPARTMENT OF DEFENSE
WASHINGTON, D.C. 20301
01CY ATTN STRATEGIC & SPACE
SYSTEMS (OS)

WWMCCS SYSTEM ENGINEERING ORG
WASHINGTON, D.C. 20305
01CY ATTN R. CRAWFORD

COMMANDER/DIRECTOR
ATMOSPHERIC SCIENCES LABORATORY
U.S. ARMY ELECTRONICS COMMAND
WHITE SANDS MISSILE RANGE, NM 88002
01CY ATTN DELAS-EO, F. NILES

DIRECTOR
BMD ADVANCED TECH CTR
HUNTSVILLE OFFICE
P.O. BOX 1500
HUNTSVILLE, AL 35807
01CY ATTN ATC-T MELVIN T. CAPPS
01CY ATTN ATC-O W. DAVIES
01CY ATTN ATC-R DON RUSS

PROGRAM MANAGER
BMD PROGRAM OFFICE
5001 EISENHOWER AVENUE
ALEXANDRIA, VA 22333
01CY ATTN DACS-BMT J. SHEA

CHIEF C-E- SERVICES DIVISION
U.S. ARMY COMMUNICATIONS CMD
PENTAGON RM 1B269
WASHINGTON, D.C. 20310
01CY ATTN C- E-SERVICES DIVISION

COMMANDER
FRADCOM TECHNICAL SUPPORT ACTIVITY
DEPARTMENT OF THE ARMY
FORT MONMOUTH, N.J. 07703
01CY ATTN DRSEL-NL-RD H. BENNET
01CY ATTN DRSEL-PL-ENV H. BOMKE
01CY ATTN J.E. QUIGLEY

COMMANDER
U.S. ARMY COMM-ELEC ENGRG INSTAL AGY
FT. HUACHUCA, AZ 85613
01CY ATTN CCC-EMEO GEORGE LANE

COMMANDER
U.S. ARMY FOREIGN SCIENCE & TECH CTR
220 7TH STREET, NE
CHARLOTTESVILLE, VA 22901
01CY ATTN DRXST-SD

COMMANDER
U.S. ARMY MATERIAL DEV & READINESS CMD
5001 EISENHOWER AVENUE
ALEXANDRIA, VA 22333
01CY ATTN DRCLDC J.A. BENDER

COMMANDER
U.S. ARMY NUCLEAR AND CHEMICAL AGENCY
7500 BACKLICK ROAD
BLDG 2073
SPRINGFIELD, VA 22150
01CY ATTN LIBRARY

DIRECTOR
U.S. ARMY BALLISTIC RESEARCH
LABORATORY
ABERDEEN PROVING GROUND, MD 21005
01CY ATTN TECH LIBRARY,
EDWARD BAICY

COMMANDER
U.S. ARMY SATCOM AGENCY
FT. MONMOUTH, NJ 07703
01CY ATTN DOCUMENT CONTROL

COMMANDER
U.S. ARMY MISSILE INTELLIGENCE AGENCY
REDSTONE ARSENAL, AL 35809
01CY ATTN JIM GAMBLE

DIRECTOR
U.S. ARMY TRADOC SYSTEMS ANALYSIS
ACTIVITY
WHITE SANDS MISSILE RANGE, NM 88002
01CY ATTN ATAA-SA
01CY ATTN TCC/F. PAYAN JR.
01CY ATTN ATTA-TAC LTC J. HESSE

COMMANDER
NAVAL ELECTRONIC SYSTEMS COMMAND
WASHINGTON, D.C. 20360
01CY ATTN NAVALEX 034 T. HUGHES
01CY ATTN PME 117
01CY ATTN PME 117-T
01CY ATTN CODE 5011

COMMANDING OFFICER
NAVAL INTELLIGENCE SUPPORT CTR
4301 SUITLAND ROAD, BLDG. 5
WASHINGTON, D.C. 20390
01CY ATTN MR. DUBBIN STIC 12
01CY ATTN NISC-50
01CY ATTN CODE 5404 J. GALET

COMMANDER
NAVAL OCEAN SYSTEMS CENTER
SAN DIEGO, CA 92152
01CY ATTN J. FERGUSON

NAVAL RESEARCH LABORATORY
WASHINGTON, D.C. 20375
01CY ATTN CODE 4700 S. L. Ossakow
26 CYS IF UNCLASS. 1 CY
IF CLASS)
01CY ATTN CODE 4701 I Vitkovitsky
01CY ATTN CODE 4780 J. Huba (50
CYS IF UNCLASS, 1 CY IF CLASS)
01CY ATTN CODE 7500
01CY ATTN CODE 7550
01CY ATTN CODE 7580
01CY ATTN CODE 7551
01CY ATTN CODE 7555
01CY ATTN CODE 4730 E. MCLEAN
01CY ATTN CODE 4108
01CY ATTN CODE 4730 B. RIPIN
20CY ATTN CODE 2628

COMMANDER
NAVAL SPACE SURVEILLANCE SYSTEM
DAHLGREN, VA 22448
01CY ATTN CAPT J.H. BURTON

OFFICER-IN-CHARGE
NAVAL SURFACE WEAPONS CENTER
WHITE OAK, SILVER SPRING, MD 20910
01CY ATTN CODE F31

DIRECTOR
STRATEGIC SYSTEMS PROJECT OFFICE
DEPARTMENT OF THE NAVY
WASHINGTON, D.C. 20376
01CY ATTN NSP-2141
01CY ATTN NSSP-2722 FRED WIMBERLY

COMMANDER
NAVAL SURFACE WEAPONS CENTER
DAHLGREN LABORATORY
DAHLGREN, VA 22448
01CY ATTN CODE DF-14 R. BUTLER

OFFICER OF NAVAL RESEARCH
ARLINGTON, VA 22217
01CY ATTN CODE 465
01CY ATTN CODE 461
01CY ATTN CODE 402
01CY ATTN CODE 420
01CY ATTN CODE 421

COMMANDER
AEROSPACE DEFENSE COMMAND/DC
DEPARTMENT OF THE AIR FORCE
ENT AFB, CO 80912
01CY ATTN DC MR. LONG

COMMANDER
AEROSPACE DEFENSE COMMAND/XPD
DEPARTMENT OF THE AIR FORCE
ENT AFB, CO 80912
01CY ATTN XPDQQ
01CY ATTN XP

AIR FORCE GEOPHYSICS LABORATORY
HANSCOM AFB, MA 01731
01CY ATTN OPR HAROLD GARDNER
01CY ATTN LKB
KENNETH S.W. CHAMPION
01CY ATTN OPR ALVA T. STAIR
01CY ATTN PHD JURGEN BUCHAU
01CY ATTN PHD JOHN P. MULLEN

AF WEAPONS LABORATORY
KIRTLAND AFT, NM 87117
01CY ATTN SUL
01CY ATTN CA ARTHUR H. GUENTHER
01CY ATTN NTYCE 1LT. G. KRAJEI

AFTAC
PATRICK AFB, FL 32925
01CY ATTN TN

AIR FORCE AVIONICS LABORATORY
WRIGHT-PATTERSON AFB, OH 45433
01CY ATTN AAD WADE HUNT
01CY ATTN AAD ALLEN JOHNSON

DEPUTY CHIEF OF STAFF
RESEARCH, DEVELOPMENT, & ACQ
DEPARTMENT OF THE AIR FORCE
WASHINGTON, D.C. 20330
01CY ATTN AFRDQ

HEADQUARTERS
ELECTRONIC SYSTEMS DIVISION
DEPARTMENT OF THE AIR FORCE
HANSCOM AFB, MA 01731
01CY ATTN J. DEAS

HEADQUARTERS
ELECTRONIC SYSTEMS DIVISION/YSEA
DEPARTMENT OF THE AIR FORCE
HANSCOM AFB, MA 01732
01CY ATTN YSEA

HEADQUARTERS
ELECTRONIC SYSTEMS DIVISION/DC
DEPARTMENT OF THE AIR FORCE
HANSCOM AFB, MA 01731
01CY ATTN DCKC MAJ J.C. CLARK

COMMANDER
FOREIGN TECHNOLOGY DIVISION, AFSC
WRIGHT-PATTERSON AFB, OH 45433
01CY ATTN NICD LIBRARY
01CY ATTN ETDP B. BALLARD

COMMANDER
ROME AIR DEVELOPMENT CENTER, AFSC
GRIFFISS AFB, NY 13441
01CY ATTN DOC LIBRARY/TSLD
01CY ATTN OCSE V. COYNE

SAMSO/SZ
POST OFFICE BOX 92960
WORLDWAY POSTAL CENTER
LOS ANGELES, CA 90009
(SPACE DEFENSE SYSTEMS)
01CY ATTN SZJ

STRATEGIC AIR COMMAND/XPFS
OFFUTT AFB, NB 68113
01CY ATTN ADWATE MAJ BRUCE BAUER
01CY ATTN NRT
01CY ATTN DOK CHIEF SCIENTIST

SAMSO/SK
P.O. BOX 92960
WORLDWAY POSTAL CENTER
LOS ANGELES, CA 90009
01CY ATTN SKA (SPACE COMM SYSTEMS)
M. CLAVIN

SAMSO/MN
NORTON AFB, CA 92409
(MINUTEMAN)
01CY ATTN MNNL

COMMANDER
ROME AIR DEVELOPMENT CENTER, AFSC
HANSCOM AFB, MA 01731
01CY ATTN EEP A. LORENTZEN

DEPARTMENT OF ENERGY
LIBRARY ROOM G-042
WASHINGTON, D.C. 20545
01CY ATTN DOC CON FOR A. LABOWITZ

DEPARTMENT OF ENERGY
ALBUQUERQUE OPERATIONS OFFICE
P.O. BOX 5400
ALBUQUERQUE, NM 87115
01CY ATTN DOC CON FOR D. SHERWOOD

EG&G, INC.
LOS ALAMOS DIVISION
P.O. BOX 809
LOS ALAMOS, NM 85544
01CY ATTN DOC CON FOR J. BREEDLOVE

UNIVERSITY OF CALIFORNIA
LAWRENCE LIVERMORE LABORATORY
P.O. BOX 808
LIVERMORE, CA 94550
01CY ATTN DOC CON FOR TECH INFO
DEPT
01CY ATTN DOC CON FOR L-389 R. OTT
01CY ATTN DOC CON FOR L-31 R. HAGER

LOS ALAMOS NATIONAL LABORATORY
P.O. BOX 1663
LOS ALAMOS, NM 87545
01CY ATTN DOC CON FOR J. WOLCOTT
01CY ATTN DOC CON FOR R.F. TASCHEK
01CY ATTN DOC CON FOR E. JONES
01CY ATTN DOC CON FOR J. MALIK
01CY ATTN DOC CON FOR R. JEFFRIES
01CY ATTN DOC CON FOR J. ZINN
01CY ATTN DOC CON FOR P. KEATON
01CY ATTN DOC CON FOR D. WESTERVELT
01CY ATTN D. SAPPENFIELD

SANDIA LABORATORIES
P.O. BOX 5800
ALBUQUERQUE, NM 87115
01CY ATTN DOC CON FOR W. BROWN
01CY ATTN DOC CON FOR A.
THORNBROUGH
01CY ATTN DOC CON FOR T. WRIGHT
01CY ATTN DOC CON FOR D. DAHLGREN
01CY ATTN DOC CON FOR 3141
01CY ATTN DOC CON FOR SPACE PROJECT
DIV

SANDIA LABORATORIES
LIVERMORE LABORATORY
P.O. BOX 969
LIVERMORE, CA 94550
01CY ATTN DOC CON FOR B. MURPHEY
01CY ATTN DOC CON FOR T. COOK

OFFICE OF MILITARY APPLICATION
DEPARTMENT OF ENERGY
WASHINGTON, D.C. 20545
01CY ATTN DOC CON DR. YO SONG

OTHER GOVERNMENT

INSTITUTE FOR TELECOM SCIENCES
NATIONAL TELECOMMUNICATIONS & INFO ADMIN
BOULDER, CO 80303
01CY ATTN A. JEAN (UNCLASS ONLY)
01CY ATTN W. UTLAUT
01CY ATTN D. CROMBIE
01CY ATTN L. BERRY

NATIONAL OCEANIC & ATMOSPHERIC ADMIN
ENVIRONMENTAL RESEARCH LABORATORIES
DEPARTMENT OF COMMERCE
BOULDER, CO 80302
01CY ATTN R. GRUBB
01CY ATTN AERONOMY LAB G. REID

DEPARTMENT OF DEFENSE CONTRACTORS

AEROSPACE CORPORATION
P.O. BOX 92957
LOS ANGELES, CA 90009
01CY ATTN I. GARFUNKEL
01CY ATTN T. SALMI
01CY ATTN V. JOSEPHSON
01CY ATTN S. BOWER
01CY ATTN D. OLSEN

ANALYTICAL SYSTEMS ENGINEERING CORP
5 OLD CONCORD ROAD
BURLINGTON, MA 01803
01CY ATTN RADIO SCIENCES

AUSTIN RESEARCH ASSOC., INC.
1901 RUTLAND DRIVE
AUSTIN, TX 78758
01CY ATTN L. SLOAN
01CY ATTN R. THOMPSON

BERKELEY RESEARCH ASSOCIATES, INC.
P.O. BOX 983
BERKELEY, CA 94701
01CY ATTN J. WORKMAN
01CY ATTN C. PRETTIE
01CY ATTN S. BRECHT

BOEING COMPANY, THE
P.O. BOX 3707
SEATTLE, WA 98124
01CY ATTN G. KEISTER
01CY ATTN D. MURRAY
01CY ATTN G. HALL
01CY ATTN J. KENNEY

CHARLES STARK DRAPER LABORATORY, INC.
555 TECHNOLOGY SQUARE
CAMBRIDGE, MA 02139
01CY ATTN D.B. COX
01CY ATTN J.P. GILMORE

COMSAT LABORATORIES
LINTHICUM ROAD
CLARKSBURG, MD 20734
01CY ATTN G. HYDE

CORNELL UNIVERSITY
DEPARTMENT OF ELECTRICAL ENGINEERING
ITHACA, NY 14850
01CY ATTN D.T. FARLEY, JR.

ELECTROSPACE SYSTEMS, INC.
BOX 1359
RICHARDSON, TX 75080
01CY ATTN H. LOGSTON
01CY ATTN SECURITY (PAUL PHILLIPS)

EOS TECHNOLOGIES, INC.
606 Wilshire Blvd.
Santa Monica, Calif 90401
01CY ATTN C.B. GABBARD
01CY ATTN R. LELEVIER

ESL, INC.
495 JAVA DRIVE
SUNNYVALE, CA 94086
01CY ATTN J. ROBERTS
01CY ATTN JAMES MARSHALL

GENERAL ELECTRIC COMPANY
SPACE DIVISION
VALLEY FORGE SPACE CENTER
GODDARD BLVD KING OF PRUSSIA
P.O. BOX 8555
PHILADELPHIA, PA 19101
01CY ATTN M.H. BORTNER
SPACE SCI LAB

GENERAL ELECTRIC COMPANY
P.O. BOX 1122
SYRACUSE, NY 13201
01CY ATTN F. REIBERT

GENERAL ELECTRIC TECH SERVICES
CO., INC.
HMES
COURT STREET
SYRACUSE, NY 13201
01CY ATTN G. MILLMAN

GEOPHYSICAL INSTITUTE
UNIVERSITY OF ALASKA
FAIRBANKS, AK 99701
(ALL CLASS ATTN: SECURITY OFFICER)
01CY ATTN T.N. DAVIS (UNCLASS ONLY)
01CY ATTN TECHNICAL LIBRARY
01CY ATTN NEAL BROWN (UNCLASS ONLY)

GTE SYLVANIA, INC.
ELECTRONICS SYSTEMS GRP-EASTERN DIV
77 A STREET
NEEDHAM, MA 02194
01CY ATTN DICK STEINHOF

HSS, INC.
2 ALFRED CIRCLE
BEDFORD, MA 01730
01CY ATTN DONALD HANSEN

ILLINOIS, UNIVERSITY OF
107 COBLE HALL
150 DAVENPORT HOUSE
CHAMPAIGN, IL 61820
(ALL CORRES ATTN DAN MCCLELLAND)
01CY ATTN K. YEH

INSTITUTE FOR DEFENSE ANALYSES
1801 NO. BEAUREGARD STREET
ALEXANDRIA, VA 22311
01CY ATTN J.M. AEIN
01CY ATTN ERNEST BAUER
01CY ATTN HANS WOLFARD
01CY ATTN JOEL BENGSTON

INTL TEL & TELEGRAPH CORPORATION
500 WASHINGTON AVENUE
NUTLEY, NJ 07110
01CY ATTN TECHNICAL LIBRARY

JAYCOR
11011 TORREYANA ROAD
P.O. BOX 85154
SAN DIEGO, CA 92138
01CY ATTN J.L. SPERLING

JOHNS HOPKINS UNIVERSITY
APPLIED PHYSICS LABORATORY
JOHNS HOPKINS ROAD
LAUREL, MD 20810
01CY ATTN DOCUMENT LIBRARIAN
01CY ATTN THOMAS POTEMRA
01CY ATTN JOHN DASSOULAS

KAMAN SCIENCES CORP
P.O. BOX 7463
COLORADO SPRINGS, CO 80933
01CY ATTN T. MEAGHER

KAMAN TEMPO-CENTER FOR ADVANCED STUDIES
816 STATE STREET (P.O DRAWER QQ)
SANTA BARBARA, CA 93102
01CY ATTN DASIAC
01CY ATTN WARREN S. KNAPP
01CY ATTN WILLIAM MCNAMARA
01CY ATTN B. GAMBILL

LINKABIT CORP
10453 ROSELLE
SAN DIEGO, CA 92121
01CY ATTN IRWIN JACOBS

LOCKHEED MISSILES & SPACE CO., INC
P.O. BOX 504
SUNNYVALE, CA 94088
01CY ATTN DEPT 60-12
01CY ATTN D.R. CHURCHILL

LOCKHEED MISSILES & SPACE CO., INC.
3251 HANOVER STREET
PALO ALTO, CA 94304
01CY ATTN MARTIN WALT DEPT 52-12
01CY ATTN W.L. IMHOF DEPT 52-12
01CY ATTN RICHARD G. JOHNSON DEPT 52-12
01CY ATTN J.B. CLADIS DEPT 52-12

MARTIN MARIETTA CORP
ORLANDO DIVISION
P.O. BOX 5837
ORLANDO, FL 32805
01CY ATTN R. HEFFNER

M.I.T. LINCOLN LABORATORY
P.O. BOX 73
LEXINGTON, MA 02173
01CY ATTN DAVID M. TOWLE
01CY ATTN L. LOUGHLIN
01CY ATTN D. CLARK

MCDONNEL DOUGLAS CORPORATION
5301 BOLSA AVENUE
HUNTINGTON BEACH, CA 92647
01CY ATTN N. HARRIS
01CY ATTN J. MOULE
01CY ATTN GEORGE MROZ
01CY ATTN W. OLSON
01CY ATTN R.W. HALPRIN
01CY ATTN TECHNICAL
LIBRARY SERVICES

MISSION RESEARCH CORPORATION
735 STATE STREET
SANTA BARBARA, CA 93101
01CY ATTN P. FISCHER
01CY ATTN W.F. CREVIER
01CY ATTN STEVEN L. GUTSCHE
01CY ATTN R. BOGUSCH
01CY ATTN R. HENDRICK
01CY ATTN RALPH KILB
01CY ATTN DAVE SOWLE
01CY ATTN F. FAJEN
01CY ATTN M. SCHEIBE
01CY ATTN CONRAD L. LONGMIRE
01CY ATTN B. WHITE
01CY ATTN R. STAGAT

MISSION RESEARCH CORP.
1720 RANDOLPH ROAD, S.E.
ALBUQUERQUE, NEW MEXICO 87106
01CY R. STELLINGWERF
01CY M. ALME
01CY L. WRIGHT

MITRE CORPORATION, THE
P.O. BOX 208
BEDFORD, MA 01730
01CY ATTN JOHN MORGANSTERN
01CY ATTN G. HARDING
01CY ATTN C.E. CALLAHAN

MITRE CORP
WESTGATE RESEARCH PARK
1320 DOLLY MADISON BLVD
MCLEAN, VA 22101
01CY ATTN W. HALL
01CY ATTN W. FOSTER

PACIFIC-SIERRA RESEARCH CORP
12340 SANTA MONICA BLVD.
LOS ANGELES, CA 90025
01CY ATTN E.C. FIELD, JR.

PENNSYLVANIA STATE UNIVERSITY
IONOSPHERE RESEARCH LAB
318 ELECTRICAL ENGINEERING EAST
UNIVERSITY PARK, PA 16802
(NO CLASS TO THIS ADDRESS)
01CY ATTN IONOSPHERIC RESEARCH LAB

PHOTOMETRICS, INC.
4 ARROW DRIVE
WOBURN, MA 01801
01CY ATTN IRVING L. KOFSKY

PHYSICAL DYNAMICS, INC.
P.O. BOX 3027
BELLEVUE, WA 98009
01CY ATTN E.J. FREMOUW

PHYSICAL DYNAMICS, INC.
P.O. BOX 10367
OAKLAND, CA 94610
ATTN A. THOMSON

R & D ASSOCIATES
P.O. BOX 9695
MARINA DEL REY, CA 90291
01CY ATTN FORREST GILMORE
01CY ATTN WILLIAM B. WRIGHT, JR.
01CY ATTN WILLIAM J. KARZAS
01CY ATTN H. ORY
01CY ATTN C. MACDONALD
01CY ATTN R. TURCO
01CY ATTN L. DeRAND
01CY ATTN W. TSAI

RAND CORPORATION, THE
1700 MAIN STREET
SANTA MONICA, CA 90406
01CY ATTN CULLEN CRAIN
01CY ATTN ED BEDROZIAN

RAYTHEON CO.
528 BOSTON POST ROAD
SUDBURY, MA 01776
01CY ATTN BARBARA ADAMS

RIVERSIDE RESEARCH INSTITUTE
330 WEST 42nd STREET
NEW YORK, NY 10036
01CY ATTN VINCE TRAPANI

SCIENCE APPLICATIONS, INC.
1150 PROSPECT PLAZA
LA JOLLA, CA 92037
01CY ATTN LEWIS M. LINSON
01CY ATTN DANIEL A. HAMLIN
01CY ATTN E. FRIEMAN
01CY ATTN E.A. STRAKER
01CY ATTN CURTIS A. SMITH

SCIENCE APPLICATIONS, INC
1710 GOODRIDGE DR.
MCLEAN, VA 22102
01CY J. COCKAYNE
01CY E. HYMAN

SRI INTERNATIONAL
333 RAVENSWOOD AVENUE
MENLO PARK, CA 94025
01CY ATTN J. CASPER
01CY ATTN DONALD NEILSON
01CY ATTN ALAN BURNS
01CY ATTN G. SMITH
01CY ATTN R. TSUNODA
01CY ATTN DAVID A. JOHNSON
01CY ATTN WALTER G. CHESNUT
01CY ATTN CHARLES L. RINO
01CY ATTN WALTER JAYE
01CY ATTN J. VICKREY
01CY ATTN RAY L. LEADABRAND
01CY ATTN G. CARPENTER
01CY ATTN G. PRICE
01CY ATTN R. LIVINGSTON
01CY ATTN V. GONZALES
01CY ATTN D. MCDANIEL

TECHNOLOGY INTERNATIONAL CORP
75 WIGGINS AVENUE
BEDFORD, MA 01730
01CY ATTN W.P. BOQUIST

TOYON RESEARCH CO.
P.O. Box 6890
SANTA BARBARA, CA 93111
01CY ATTN JOHN ISE, JR.
01CY ATTN JOEL GARBARINO

TRW DEFENSE & SPACE SYS GROUP
ONE SPACE PARK
REDONDO BEACH, CA 90278
01CY ATTN R. K. PLEBUCH
01CY ATTN S. ALTSCHULER
01CY ATTN D. DEE
01CY ATTN D/ STOCKWELL
SNTF/1575

VISIDYNE
SOUTH BEDFORD STREET
BURLINGTON, MASS 01803
01CY ATTN W. REIDY
01CY ATTN J. CARPENTER
01CY ATTN C. HUMPHREY

UNIVERSITY OF PITTSBURGH
PITTSBURGH, PA 15213
01CY ATTN: N. ZABUSKY

DIRECTOR OF RESEARCH
U.S. NAVAL ACADEMY
ANNAPOLIS, MD 21402
02CY

END

FILMED

8-85

DTIC